Microstructure-induced anisotropic tribological properties of Sc-Zr modified Al–Mg alloy (Scalmalloy®) produced via laser powder bed fusion process

Original
Microstructure-induced anisotropic tribological properties of Sc-Zr modified Al–Mg alloy (Scalmalloy®) produced via laser powder bed fusion process / Abdi, A., Salehi, M.S., Fatemi, S.A., Iuliano, L., Saboori, A.. - In: INTERNATIONAL JOURNAL, ADVANCED MANUFACTURING TECHNOLOGY. - ISSN 0268-3768. - 130:1-2(2024), pp. 755-779. [10.1007/s00170-023-12691-5]

Publisher:
Springer Science and Business Media Deutschland GmbH

Published
DOI:10.1007/s00170-023-12691-5

The International Journal of Advanced Manufacturing Technology (2024) 130:755–779
https://doi.org/10.1007/s00170-023-12691-5

ORIGINAL ARTICLE

Microstructure-induced anisotropic tribological properties of Sc-Zr modified Al–Mg alloy (Scalmalloy®) produced via laser powder bed fusion process

Ata Abdi[1] · **Majid Seyed Salehi**[1] · **Seyed Ali Fatemi**[2] · **Luca Iuliano**[3] · **Abdollah Saboori**[3]

Received: 24 July 2023 / Accepted: 15 November 2023 / Published online: 2 December 2023

Abstract

In this study, the correlation between the microstructure and tribological performance of Sc and Zr-modified Al–Mg alloy (Scalmalloy®) samples produced via laser powder bed fusion process was evaluated via a dry sliding Pin-on-Disc wear test under different planes, directions, and various normal applied loads. The results revealed a remarkable dependency of wear properties on the as-built microstructure so that different behaviors were observed along the scanning and building planes. The microstructural examination indicated the presence of bi-modal grains and finely shaped equiaxed grains observed in the building and scanning planes, respectively. Increasing the applied loads from 20 to 40 N led to a significant increase in the coefficient of friction (COF) while increasing the load from 40 to 60 N, slightly decreasing the COF for the studied samples. No dependency was found between the COF and the corresponding microstructure at the highest applied load. The anisotropic wear resistance and COF values were predominant at the lowest applied load. Due to tailored as-built microstructural features and different microhardness values, lower wear rates were noticed along the scanning plane for all applied loads. Under the 20 N applied load, however, the worn surface of the scanning plane showed a clearer and smoother surface compared to the building plane surfaces. Ultra-fine equiaxed grains along the scanning plane and columnar grains along the building plane were determined as the main factors creating anisotropic tribological behavior. The outcomes of this study can pave the way toward producing more wear-resistant surfaces and developing components for critical wear applications in as-built conditions with no need for expensive and time-consuming surface treatments.

Keywords Additive manufacturing · Laser powder bed fusion · Scalmalloy® · Anisotropy · Dry sliding wear · Coefficient of friction

1 Introduction

Metal additive manufacturing (AM) introduces a new perspective for manufacturing in different industries [1, 2]. The benefits of metal AM processes include but are not limited to the toolless and modeless manufacturing of complicated geometries with low-volume raw material consumption [3, 4]. Decreasing the assembly steps, eliminating weld joints, and building several components into one integrated part can be considered the other advantages of the metal AM processes [5, 6]. During the past decade, laser powder bed fusion (L-PBF), also known as selective laser melting (SLM) together with the electron beam melting (EBM) method, are two well-known PBF methods receiving much attention from the academia and industry [7, 8]. In the L-PBF method, to obtain integrated parts, a laser is used as a heat source to melt a thin metal powder layer spread by a recoating roller onto a building platform [9, 10]. It is well documented that microstructure type and properties of as-built L-PBF parts mainly depend on the thermal history involved in the process due to rapid solidification (10^5–10^7 K/s) [11, 12]. This exotic thermal history can be attributed to process parameters such as laser power, laser scanning speed, hatching distance, scan

✉ Abdollah Saboori
abdollah.saboori@polito.it

[1] Faculty of Materials Science and Engineering, K. N. Toosi University of Technology, Tehran 19395-1999, Iran

[2] Faculty of Mechanical Engineering, Toosi University of Technology, Tehran 19395-1999, K. N, Iran

[3] Integrated Additive Manufacturing Center (IAM), Department of Management and Production Engineering, Politecnico Di Torino, Corso Duca Degli Abruzzi, 24, 10129 Turin, Italy

strategy, building platform temperature, and layer thickness [13–15]. L-PBF technology has proven to be a reliable and promising metal AM technology, ensuring the industrial and end-user quality of complex parts with a novel industrial design [16, 17]. According to European Union (EU) laws, the automotive sector must significantly decrease automobile weight to reduce harmful emissions and increase fuel efficiency from 2025 to 2030 [18]. As a general guideline, fuel savings of 4% may be accomplished by lowering the vehicle's mass by 10% [19]. To address this requirement, L-PBF can be proposed as a promising solution in which engineering components can be produced by light alloys and designed by topology optimization rules to achieve a lightweight product at a lower cost.

Therefore, L-PBF of high-performance aluminum alloys with high structural integrity and low density is being increased to replace ferrous components, especially in the transportation industries [20]. In contrast, aluminum structural components made by conventional manufacturing methods such as casting, extrusion, and powder metallurgy (PM) have coarser grains and less desirable mechanical properties than their L-PBF counterparts [21, 22]. Accordingly, additive manufacturing of aluminum alloys in the transportation industries is prevalent not only for producing lightweight components with design freedom but also for peculiar microstructure and reliable mechanical properties. These key factors made aluminum alloys known as the third most studied L-PBF metal [23, 24]. Despite the mentioned advantages, L-PBF of aluminum alloys suffers from some challenges, including a somewhat difficult flow of a few microns of powder layer, high laser power due to low laser energy absorption and high thermal conductivity, poor wettability due to the formation of thin oxide layers around the molten pool of successive layers [25, 26].

Notwithstanding former challenges, adding rare earth elements such as scandium (Sc) and zirconium (Zr) to aluminum alloys gained much interest due to their significant chemical stability and higher mechanical strength [27]. The underlying challenges experienced during the L-PBF processing of aluminum alloys, along with the positive effects of Sc and Zr addition, led to the compositions designed explicitly for L-PBF, i.e., Scalmalloy® RP [28] and Addalloy® 5T (an Sc-free Al–Mg-Zr ternary Al alloy) [29, 30]. Scalmalloy® was officially invented in 2007 by Airbus Group APWorks GmbH, Germany, in cooperation with Airbus Group R&D as a new Sc- and Zr-modified Al–Mg alloy optimized for L-PBF processing. Scalmalloy® is as light as the well-studied AlSi10Mg aluminum alloy but has more microstructural stability at higher temperatures with better corrosion resistance while being featured with ductility and strength close to Ti6Al4V alloy at the same time [31]. Therefore, it can be considered an excellent candidate to utilize in the transportation industry. In recent years, microstructural features and mechanical properties of Scalmalloy® produced by L-PBF have been widely investigated. In 2011, Schmidtke et al. [32] reported excellent processability for L-PBF Al–Mg alloy containing Sc and Zr (Al-4.5Mg-0.7Sc-0.4Zr-0.5Mn) for the first time. Another study by Spierings et al. [33], who successfully produced dense Scalmalloy® samples via the L-PBF process, reported an inhomogeneous microstructure featured by columnar grains inside the melt pool (MP) and fine equiaxed grains along the MP boundaries (MPBs). In another research, Awd et al. [34] reported that the fatigue and tensile strength of Scalmalloy® produced by L-PBF and laser metal deposition (LMD) were higher than AlSi10Mg. Recently, Muhammad et al. [35] reported that L-PBF Scalmalloy® could be considered a highly fatigue-resistant alloy with the highest tensile strength among the investigated aluminum alloys. Interestingly, Spierings et al. [36] revealed that the microstructure of L-PBF Scalmalloy® was not affected significantly by post-heat treatment and preserved its as-built mechanical properties even up to 300 °C due to the presence of particles that are pinning the grain boundaries. Therefore, as-built mechanical properties of L-PBF Scalmalloy® at room temperature, such as its dry sliding wear performance, are essential and should be addressed deeply.

Notably, wear is not an intrinsic material property but depends on a tribological system. During its service, a complex part may undergo substantial loading and friction in different angles and planes concerning the AM building direction. On the other hand, in aluminum alloys, anodizing is widely used to improve wear resistance and corrosion protection. However, due to the high geometrical complexity often observed in the AM parts and the limited access to all surfaces, traditional surface treatment such as coating or sandblasting may be challenging and faced with difficulty [37–39]. Therefore, the as-built wear properties of 3D-printed aluminum components must be deeply addressed. Thus, for reducing the whole manufacturing steps and removing post-processing procedures, saving time, cost, and energy, modifying the microstructure of as-built additively manufactured parts appears to be a viable strategy [40].

Consequently, the profound effect of L-PBF as-built microstructure on the wear behavior of additively manufactured alloys has been investigated in the literature. Zhang et al. [41] revealed that scan speed significantly impacts the wear behavior of Al–Mg-Sc-Zr alloy. Enhanced wear performance and higher microhardness were reported in their work, thanks to the precipitation of the coherent Al_3(Sc, Zr) phase when the laser scan speed was decreased. Tocci et al. [42] demonstrated that the additively manufactured Scalmalloy® exhibited a lower wear rate (0.9×10^{-3} $mm^3/N \cdot m$) after the same sliding distance in comparison with the widely studied AlSi10Mg alloy (1.80×10^{-3} $mm^3/N \cdot m$) produced by the same technology [43]. Moreover, they showed an adhesive wear mechanism after annealing treatment (325 °C for 4 h) via formation and fragmentation of the oxide layer by increasing sliding distance, which was predominant in Scalmalloy®.

Although it has been shown that Scalmalloy® is an isotropic alloy in terms of its tensile strength [32], studies addressing the anisotropic wear performance of this alloy along the building and scanning planes are seldom in the literature. Some published studies reported that the as-built microstructure of L-PBF alloys showed anisotropy in their wear properties. In different scan strategies, Mishra et al. [44] showed anisotropic wear behavior at the scanning and building planes of the additively manufactured AlSi10Mg alloy. Their study showed that the best wear rate and coefficient of friction (COF) values in the building plane with the island scan strategy are achievable instead of the continuous scan strategy. Yang et al. et al. [45] revealed a microstructural-induced anisotropic wear behavior in three different surfaces (top, front, and side) of the L-PBF 316L stainless steel sample produced via a zigzag scanning strategy. The authors found that wear anisotropy was predominant under a low applied load, and the best wear resistance was achieved on the side surface perpendicular to the columnar grains axis. In another study, Bahshwan et al. [46] showed that the wear rate of L-PBF 316L stainless steel decreased by increasing the applied loads citing the work-hardening effect. Besides, they found that L-PBF process-induced porosities did not profoundly affect the wear resistance, and high angle grain boundaries' interactions in contact area played a vital role in wear performance even at equal hardness values.

Nevertheless, according to the literature review, there is no specific study on the microstructural-induced anisotropic tribological properties of Scalmalloy® produced via L-PBF. As a result, it is critical to establish the effect of the as-built microstructure on the microhardness and wear resistance, significantly contributing to the service performance of as-built L-PBF Scalmalloy®. Thus, this work aims to fill the mentioned research gap and unveil the anisotropic wear behavior despite isotropic tensile properties of L-PBF Scalmalloy®. To this aim, scanning and building planes and different directions were chosen. The relationship between optimum L-PBF process parameters, the resulting microstructure, and wear resistance under different applied loads will be discussed further. Moreover, the following sections will investigate the remarkable effects of microstructural aspects on the COF and wear mechanisms. Findings in this study pave the way for a better understanding of the microstructural effects on the tribological properties of as-built L-PBF Scalmalloy®, which can be advantageous in the design for additive manufacturing (DfAM) of industrial complex components subjected to complex dry sliding wear services.

2 Materials and methods

2.1 Starting material

This work used a gas-atomized spherical Sc-Zr modified Al–Mg Alloy powder with a particle size range of ~15–45 µm as feedstock material. The nominal chemical composition of this alloy is reported in Table 1.

Figure 1 a and b show the morphology of the starting powder in this work. As can be seen, most of the powder particles are spherical and consist of some agglomeration and satellites on the surface of the larger particles, typical defects that can be revealed in the gas atomized powders.

2.2 Sample production

This research produced cubes of 15 × 15 × 15 mm^3 using an SLM 280 machine of L-PBF solutions. The samples were produced on an Al building platform using a laser power of 500–700 W at 1200–1700 mm/s speed. During the build, the chamber was kept under argon gas, and each layer was rotated 67° concerning the previous layer (Fig. 2a). For easy sample removal, all the cubic samples were built on the support structures, as shown in Fig. 2b (yellow dotted line). Before sample production, the feedstock material was dried at 80 °C for 4 h to remove the possible humidity from the powder particles.

2.3 Microstructural characterization

All samples were ground and mechanically polished for microstructural characterization and followed by etching using Keller's reagent (1% HF–1.5%HNO_3–1.5%HCl–30 ml distilled water) for 5–8 s. An optical microscope (OM) and a field emission scanning electron microscopy (FESEM-MIRA3 TESCAN) were employed to identify the microstructural features, MPs, grain size, grain morphology, and worn surfaces. Besides, the energy-dispersive X-ray spectroscopy (EDS-SAMX) technique was utilized to perform elemental analysis by incorporating the standard PAP correction. Moreover, X-ray diffraction analysis (Rigaku Ultima

Table 1 The nominal chemical composition of Sc-Zr modified Al–Mg Alloy powder

Sc-Zr modified Al–Mg alloy	Sc	Mg	Zr	Si	Fe	Cu	Mn	Zn	Ti	V
Composition (wt%)	0.68	4.25	0.41	0.33	0.2	0.04	0.68	0.19	0.07	0.05

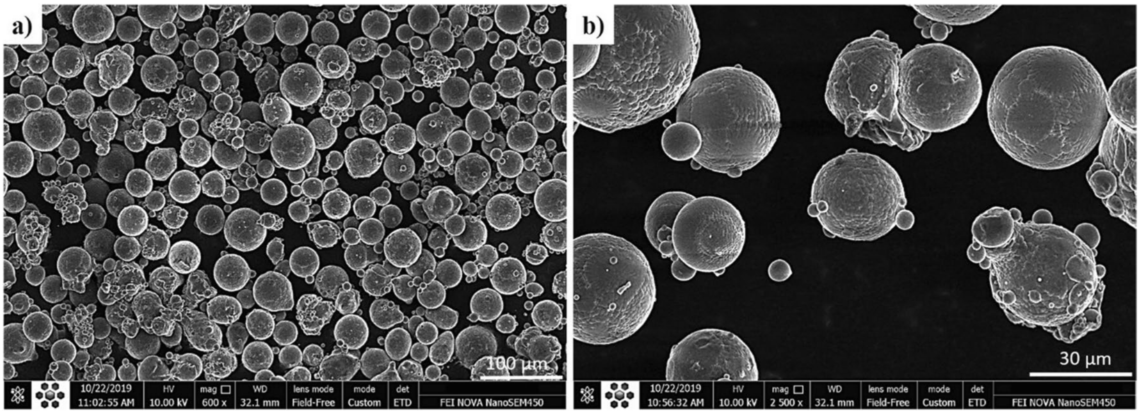

Fig. 1 FE-SEM micrograph of the Sc-Zr modified Al–Mg Alloy particles used in this work: (a) spherical morphology, (b) higher magnification from (a)

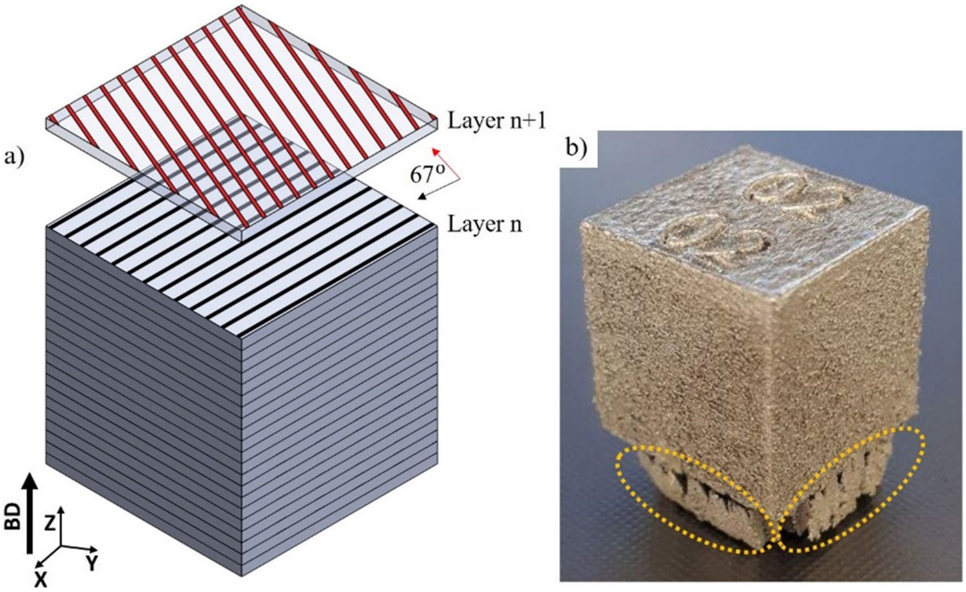

Fig. 2 As-built Sc-Zr modified Al–Mg Alloy cube; **a** schematic of scanning strategy and 67° rotation between each layer during the L-PBF process; **b** As-built cubic sample ($15\times15\times15$ mm^3). Yellow dotted lines indicate support structures

IV diffractometer with Cu-k$_\alpha$ radiation, 40 kV and 40 mA) was employed using the 4° scan step size in a wide range of 5–100° (2θ) for the phase analysis of as-fabricated L-PBF Scalmalloy®.

2.4 Dry sliding wear tests

Wire electrode discharged machining (WEDM) was used to remove the support structure from the as-fabricated Scalmalloy® (Fig. 2b) and then cut the as-fabricated sample into the nine ($5\times5\times5$ mm^3) samples (Fig. 3). These tiny cubes were used as pins for the pin-on-disc test. The micro-Vickers hardness test (ASTM E384 standard method) [47] was performed (load: 0.5 N, dwelling time: 15 s) using a Buehler Vickers micro-hardness tester at different mirror-like polished sections.

According to ASTM G 99–05 standard [48], a tribometer equipment (AMI Wear Test Machine) was employed to conduct the dry sliding wear test at room temperature in the air, as schematically illustrated in Fig. 4. For this purpose, an AISI 52100-bearing-steel disc with a hardness of 60 HRC was used as the counterface material. Before the wear tests, both counterface and pins were grounded with 1500 grit sandpaper to eliminate the contaminants, oxides, and the recast layer from the pins. All flatted-head pins were cleaned in an ultrasonic bath for 5 min before and after the wear test. Weight loss was measured by weighing the specimens (with 10^{-4} g accuracy) before and after the wear test. The wear test equipment automatically calculated and recorded the COF during the whole process for each sample.

The wear tests were performed under three applied loads of 20, 40, and 60 N, with a constant linear sliding speed of

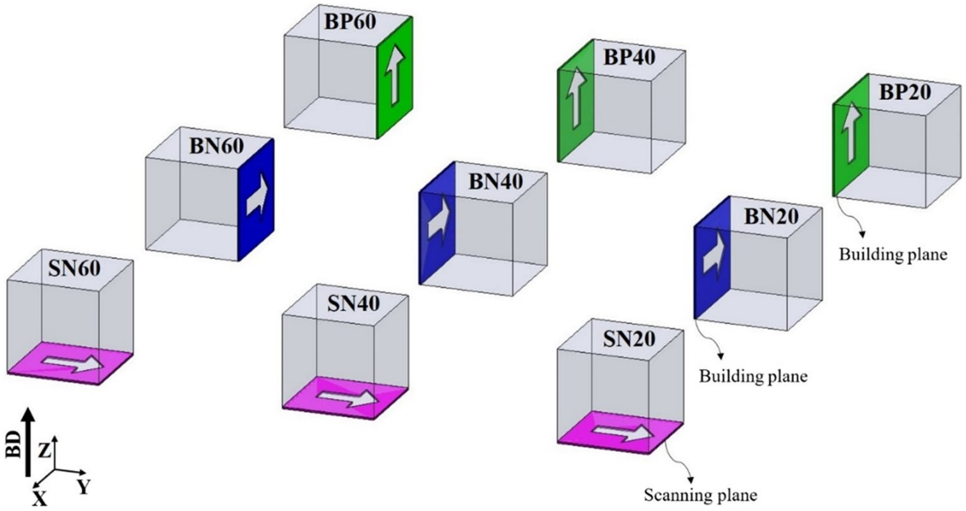

Fig. 3 Schematic of experiment design and sample designation for dry sliding wear tests. The BD arrow shows the building direction and colorful planes, indicating the dry sliding wear planes and directions, respectively

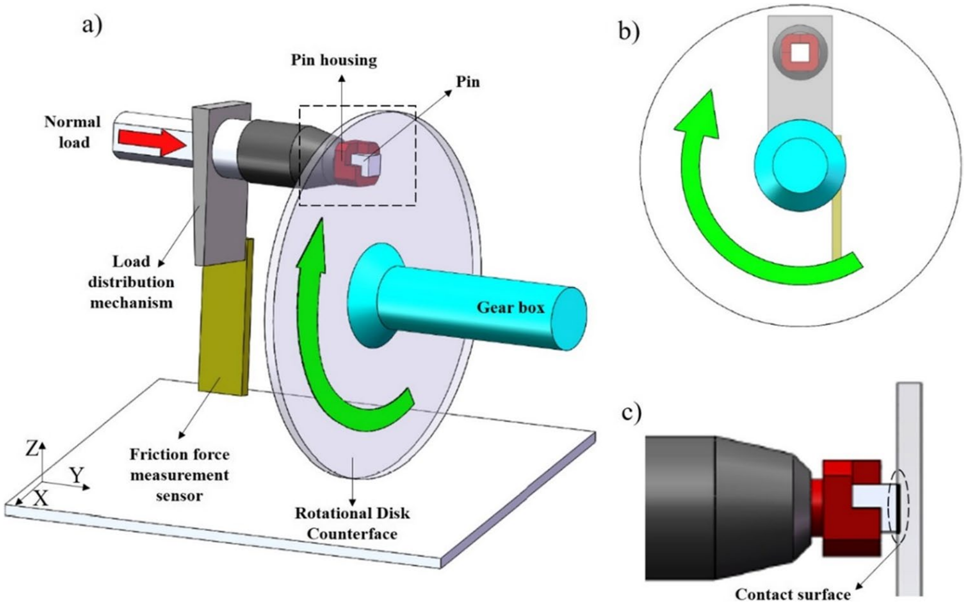

Fig. 4 Schematic of wear test machine components. (b) Side view of (**a**) in *XZ* plane. (c) Contact surface in higher magnification of dashed region in the *ZY* plane in (a)

100 cm/s and a sliding distance of 2500 m. The volume loss parameter (V_{loss}) was measured according to Eq. (1):

$$V_{loss} = M_{loss}/\rho \tag{1}$$

where M_{loss} is the weight loss; and ρ is the density of the material. Accordingly, the normalized/volumetric wear rate can be calculated as

$$W = V_{loss}/L \tag{2}$$

where L is the total sliding distance.

To make a more accurate comparison of the wear properties of all nine samples, shown in Fig. 3, the interior planes were chosen for dry sliding wear tests, with the exterior surfaces of the as-fabricated sample being ignored in this study. The sample designation and dry sliding wear test parameters are represented in Table 2. The first and the second characters of the sample's names denote the sliding planes (S: scanning plane and B: building plane) and direction (N: normal to building direction and P: parallel to building direction), respectively. Therefore, the SN refers to the samples used for dry sliding wear tests along the scanning plane and normal direction to the reference build direction (BD), i.e., Z-direction. Moreover, the BN is related to those samples used for dry sliding wear tests in the building plane and normal direction to the Z-direction. Eventually, the BP was considered for those samples used for dry sliding wear tests in the building plane and parallel to the Z-direction. The number on the right side of the sample name declares the Newton normal sliding force.

Due to the scan strategy and 67° rotation between the layers during the L-PBF process, an arbitrary direction (e.g.,

Table 2 Design of experiments and dry sliding wear test parameters according to Fig. 3

Sample no	Plane designation	Wear test direction	Normal applied load (*N*)
SN20	Scanning plane	Normal to the building direction	20
SN40			40
SN60			60
BN20	Building plane	Normal to the building direction	20
BN40			40
BN60			60
BP20	Building plane	Parallel to the building direction	20
BP40			40
BP60			60

normal to building direction) was considered for dry sliding wear tests of SN samples. However, for evaluating the anisotropic tribological properties, the same dry sliding wear tests were performed for the building plane in different directions, perpendicular (BN samples) and parallel (BP samples) to the building direction), i.e., *Z*-direction.

3 Results and discussion

3.1 Microstructural analysis

Figure 5 shows the optical micrograph that includes some interior process-induced defects. In Fig. 5 a, the red arrows indicate small porosities (~ 10 μm) observed in the sample.

These porosities were formed due to internal gas bubbles trapped in the molten metal during the L-PBF of aluminum alloys, which could not exit from the molten pool due to the high solidification rate in the L-PBF process. Hence, the formation of spherical porosities can be expected. Furthermore, moisture or already existing pores (entrapped hydrogen) in the feedstock and excess argon, nitrogen, and oxygen solved into the molten material may also promote the formation of gas porosities [49, 50].

In Fig. 5 b, some unmelted Scalmalloy® powders and unconsolidated materials can be seen in narrow disc-like lack of fusion (LOF) porosity with irregular morphology (~ 40 μm). These defects may be attributed to forming of thin oxide films in the aluminum liquid during the SLM processing of aluminum alloy. These double films have no bonding between adjacent laser tracks, and consequently, the trapped unmelted Scalmalloy® powder particles can be expected [51–54].

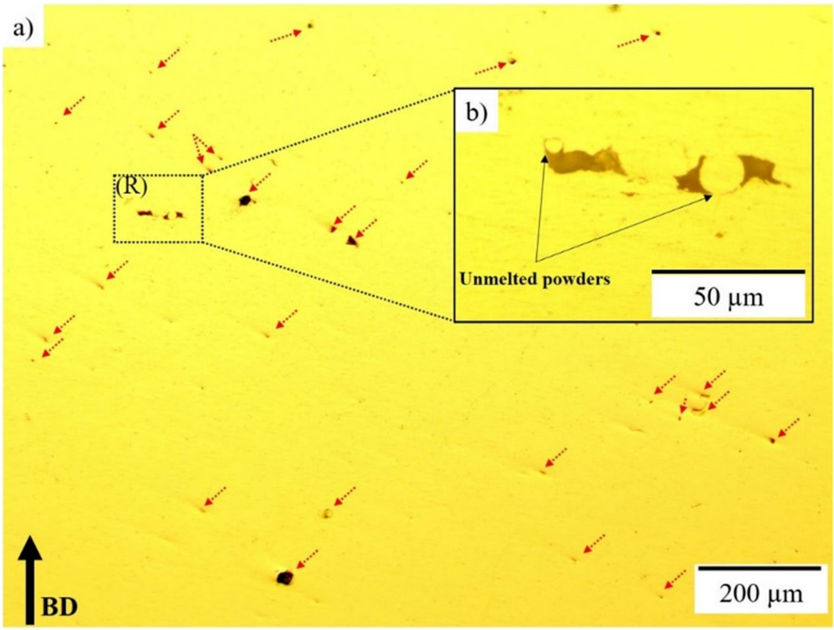

Fig. 5 Optical as-polished micrograph of the building plane of the as-fabricated sample. (a) The red arrows indicate some common defects (pores and LOF). (b) Higher magnification of region R in (a); black arrows indicate unmelted powders within LOF

A 3D optical micrograph of the as-fabricated L-PBF Scalmalloy® sample is shown in Fig. 6 a. Figure 6 b and c demonstrate the building and scanning plane microstructures at higher magnification, respectively. The layer-wise manufacturing and alternation of melt tracks in the building plane are manifested along with lenticular-shape (crescent shape) molten pools (~ 110 μm in width and ~ 90 μm in depth) (Fig. 6b). It can be realized that the depth of the MPs is higher than the first-determined powder layer thickness for the L-PBF machine (30 μm). It can be attributed to re-melting the previously solidified layers (two to three layers).

Moreover, the microstructure consists of many overlapped MPs depending on the defined hatch distance spacing parameter (h), shown with a dashed line in Fig. 6 b. On the other hand, in Fig. 6 c, laser scan tracks with 67° rotation between layers in the scanning plane reveal higher width (~ 120 μm) than laser spot size, corresponding to the material thermal conductivity under laser exposure [55, 56].

Further investigations were performed on L-PBF Scalmalloy® samples by FE-SEM on both scanning and building planes, as presented in Fig. 7. The results showed that the microstructure in the scanning plane (Fig. 7a) contained refined equiaxed grains arranged along the laser scanning path with a mean size of ~ 1–5 μm. Besides, the dashed-line area in Fig. 7 a shows the scanning laser path and a gradient in grain size from the ultra-fine equiaxed grains (UFEGs) at the edge (~ below 1 μm–point 1) (Fig. 7c), to the coarser grains at the center (~ below 5 μm–point 5) (Fig. 7b). This difference can be attributed to a partially higher cooling rate at the edge of the laser path.

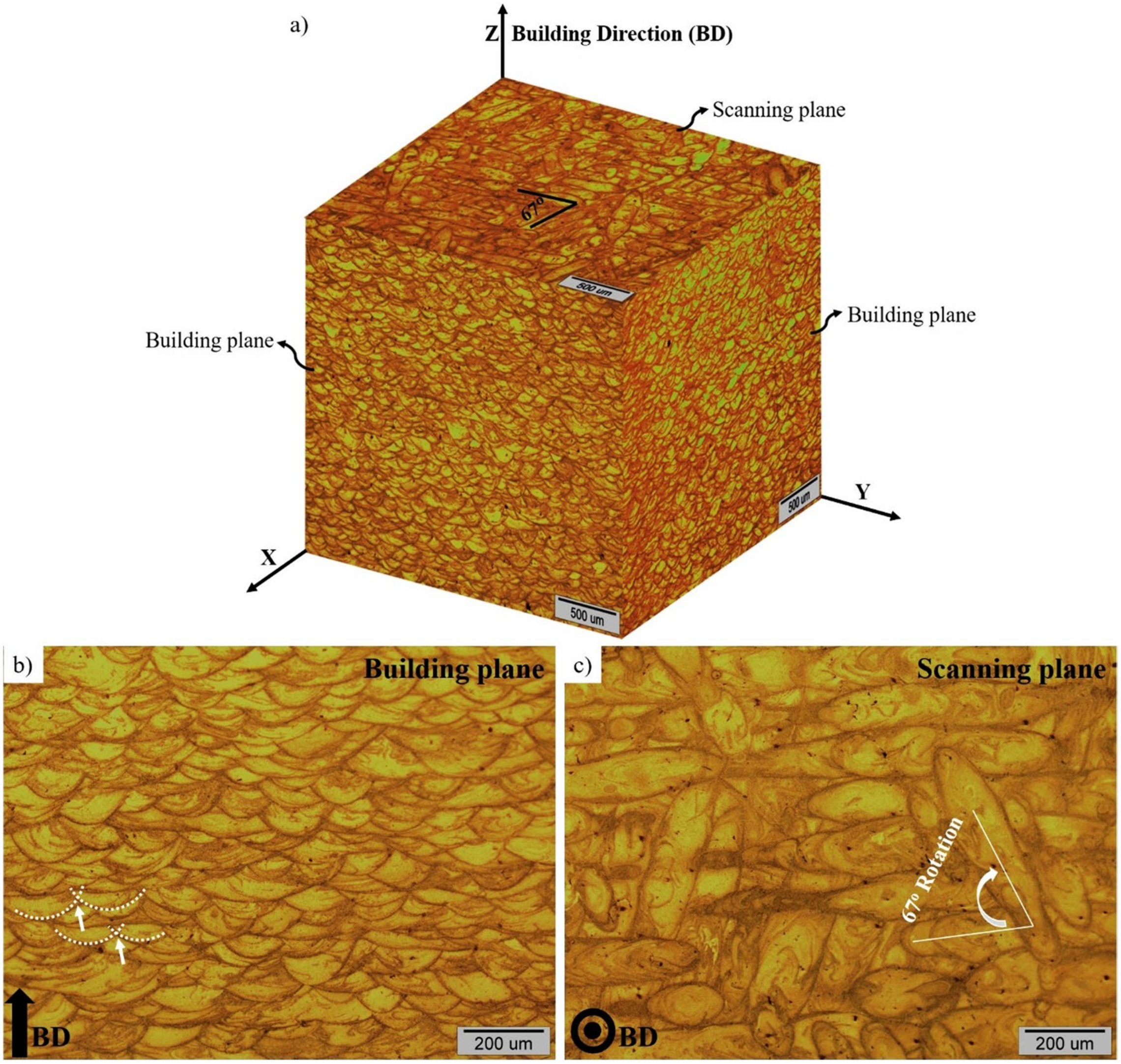

Fig. 6 The optical microscopic microstructure of etched sample. (a) Three-dimensional demonstration of the as-built sample, (b) building plane, and (c) scanning plane. White arrows in (b) indicate interaction points of adjacent molten pools. The white arrow in (c) indicates 67° rotation between successive layers

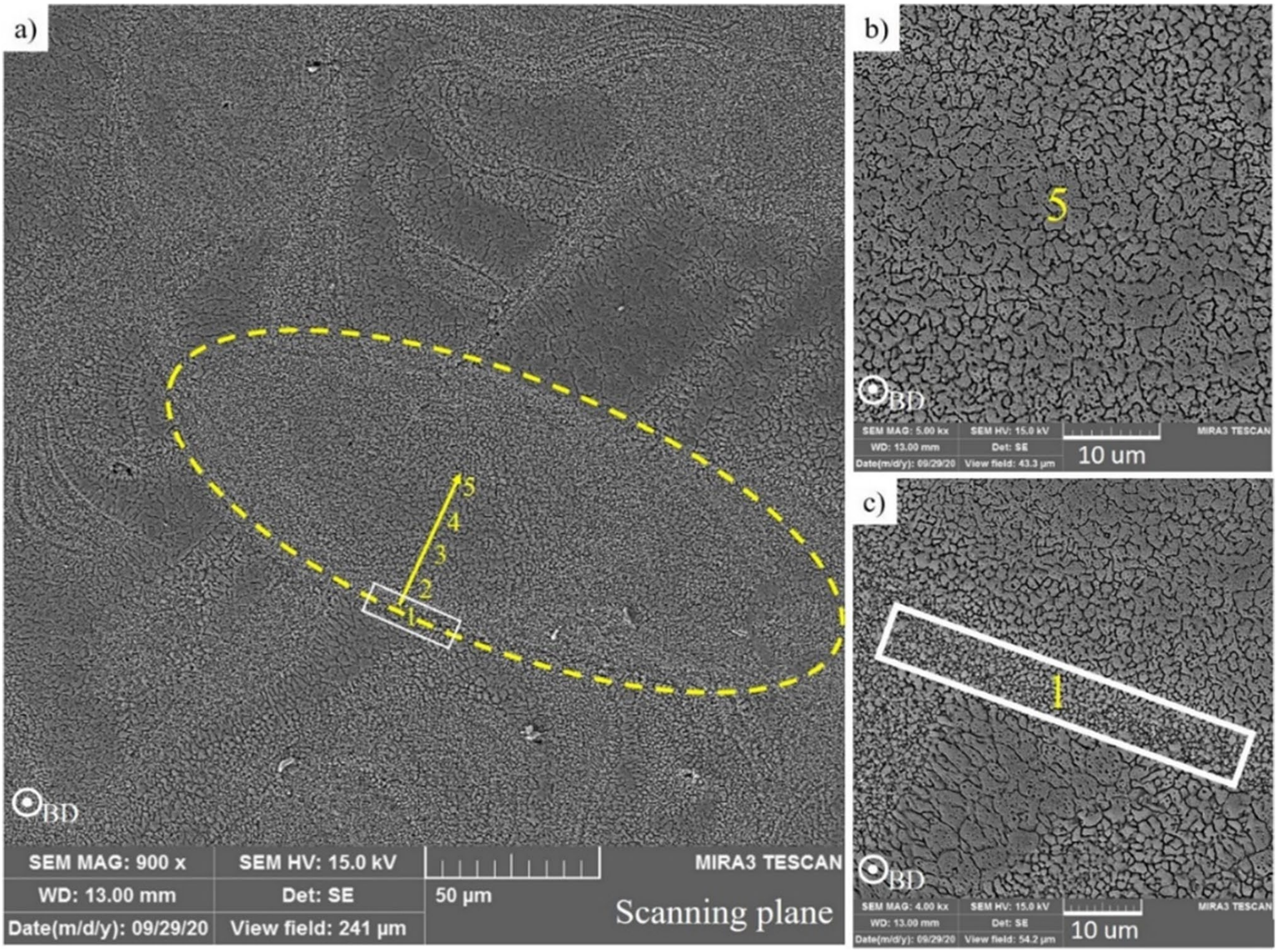

Fig. 7 FE-SEM analysis from scanning plane, (a) dashed-line indicates a laser scan path and a gradient in grain size by numbering from ultra-fine equiaxed grains (UFEGs) in edge (point 1) to the coarser center (point 5), (b) higher magnification of point 5 in (a), and (c) higher magnification of point 1 in (a)

Figure 8 a shows the microstructure along the building plain with successive overlapping laser tracks and MPs by specific boundaries. Moreover, the elongated columnar grains (CGs) with ~ 20–40 µm long can be seen inside a molten pool (Fig. 8b). This grain growth resulted in multiple columnar grains being oriented toward the maximum thermal gradient on the top surface of the MPs [57]. Due to a high thermal gradient toward the surface of the MP and deficiency of $Al_3(Sc, Zr)$ precipitates inside the MP, the formation of CGs was promoted [58]. The lack of nucleation in the CGs' region can be attributed to the Zr and Sc solute trapping from increasing solidification front velocities toward the MP surface [29].

Interestingly, many nano-sized grains and UFEGs were observed throughout the MP boundaries, which can be attributed to the initiation of grain nucleation from nano-sized $Al_3(Sc, Zr)$ precipitates on the MP boundaries, which can promote a high grain refinement degree [59]. Consequently, columnar grains were generally limited within the molten pools [60]. The presence of $Al_3(Sc, Zr)$ precipitates can be verified by regional EDS analysis of the center of an MP (region A) and its boundary (region B), which are shown in Fig. 8 c, d.

As can be seen, the boundary region is enriched more in Zr, O, and Mn compared to the center of the MP. The higher amount of these elements can be attributed to $Al_3(Sc, Zr)$ precipitate and Al–Mg oxides particles along the MPBs and the formation of UFEGs bands [41]. The SEM–EDS map of Fig. 8 b can be seen in Fig. 9 b. However, the SEM–EDS map revealed a homogeneous distribution of alloying elements along the building plane. SEM–EDS map further showed the same uniform alloying elements distribution for the scanning plane. The difference between regional EDS analysis and the EDS map can be attributed to the detection limit in the EDS map, in which no significant segregation of Sc, Zr, and O elements was observed. However, regional

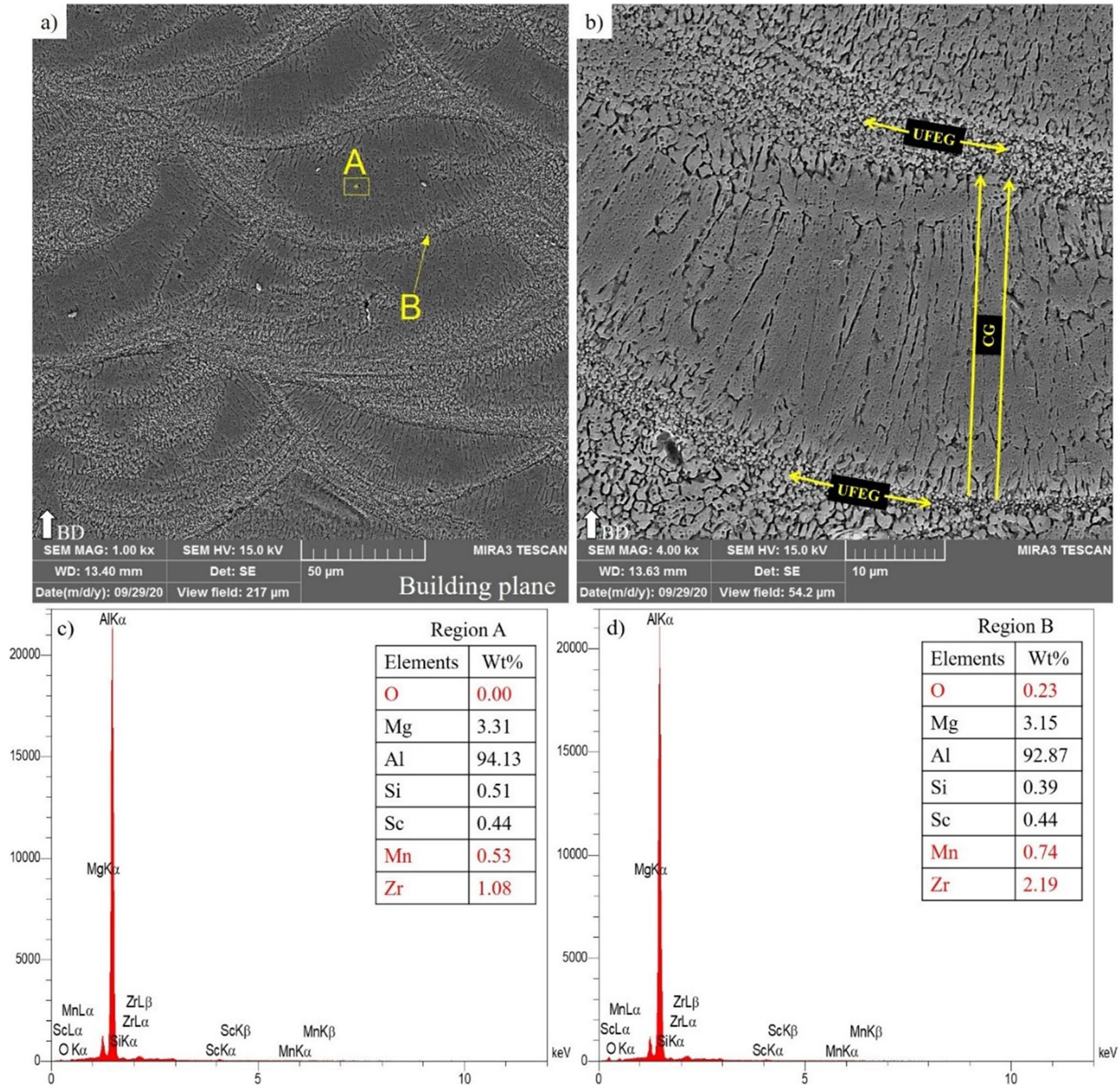

Region A

Elements	Wt%
O	0.00
Mg	3.31
Al	94.13
Si	0.51
Sc	0.44
Mn	0.53
Zr	1.08

Region B

Elements	Wt%
O	0.23
Mg	3.15
Al	92.87
Si	0.39
Sc	0.44
Mn	0.74
Zr	2.19

Fig. 8 FE-SEM characterization of building plane, (b) higher magnification of (a), (c) regional EDS analysis of region A in (a), and (d) regional EDS analysis of region B in (a)

EDS analysis (Fig. 8c, d) revealed this segregation from a qualitative comparison viewpoint.

Moreover, another study showed that the Scanning transmission electron microscopy (STEM) equipped with a high-angle annular dark-field (HAADF) detector had confirmed the presence of nano-size Al_3(Sc, Zr) and Al–Mg oxide particles along the MPBs in UFEGs' bands [58]. Consequently, the differences between microstructure in CGs' and UFEGs' regions might be due to chemical composition distribution and the higher cooling rate along the MPBs. These microstructural findings reveal that Sc and Zr elements, steep thermal gradient, and a high solidification rate significantly affect the final microstructure of L-PBF Scalmalloy®.

The XRD pattern of the as-built sample in both building and scanning planes is shown in Fig. 9 a. The peaks related to the α-Al (fcc) phase were detected, and no distinct phase transformation was observed. The diffraction peak of the Al_3Sc phase was not detected, although it can be formed via post-heat treatment at elevated temperatures by increasing the Al_3Sc precipitate density [36, 61].

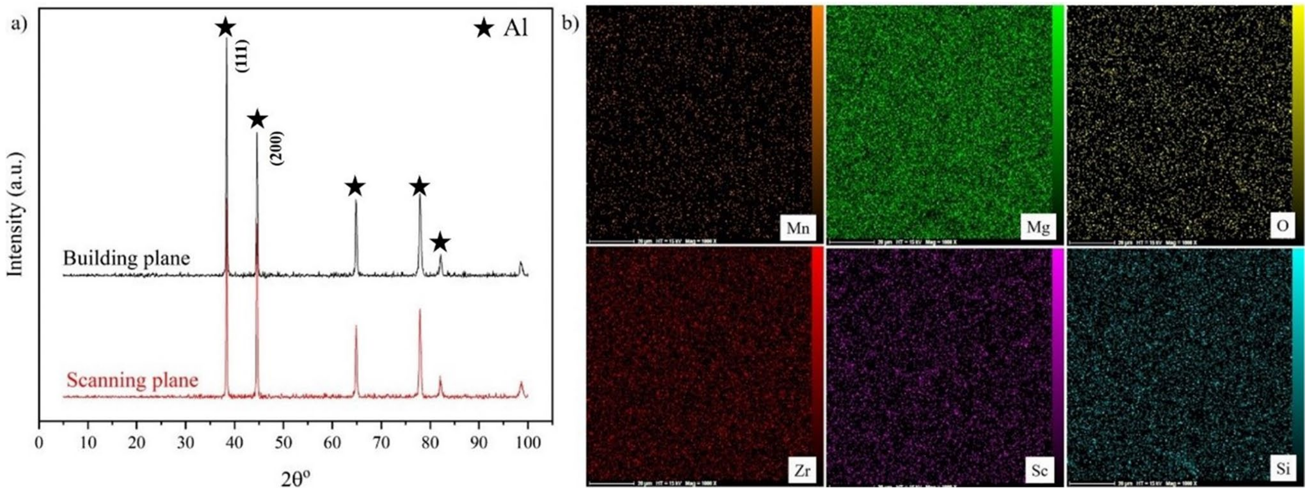

Fig. 9 **A** XRD spectra of as-built Scalmalloy® from scanning and building planes. **b** SEM–EDS mapping of the building plane (Fig. 8b)

3.2 Tribological and microhardness properties

3.2.1 Microhardness

Vickers microhardness results of the scanning plane and building plane demonstrate the effect of the as-built microstructure on the microhardness distribution of Scalmalloy®, Fig. 10. Microhardness was measured at 20 points with constant intervals along the *X* and *Y*-axes in the scanning plane (Fig. 10a), and *Y* and *Z*-axes in the building plane (Fig. 10b). Compared to the hardness value resulting for the building plane, 89.5 HV on average, the results indicate a higher microhardness value of 95.2 HV on average in the scanning plane. Also, the scanning plane shows a more homogeneous hardness with lower fluctuation across the data points when compared with the building plane. Higher dislocation density accompanied by higher grain boundary area results in a higher microhardness value of a fine microstructure than coarser ones, supported by the Hall–Petch relationship [62]. Specifically, the lower microhardness in the building plane can be attributed to the coarsened microstructure localized inside the MPs. According to the Archard equation, hardness is inversely proportional to wear volume [63], significantly influencing the wear rate [64]. Hence, hardness can be considered an effective parameter and indicates a higher wear resistance in the scanning plane than in the building plane [65–67]. This finding is further backed by more data analysis and microstructural characterization in the following sections.

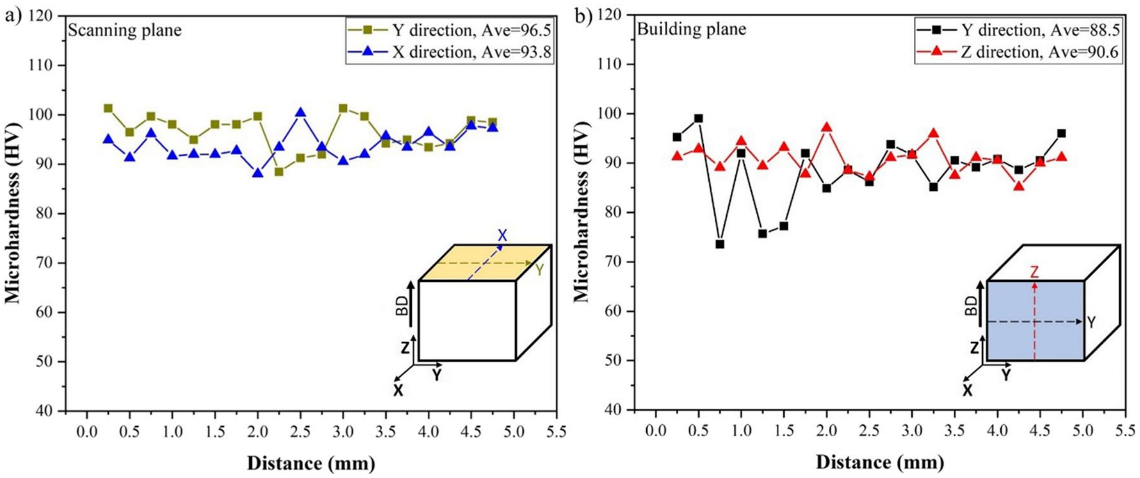

Fig. 10 Variation of microhardness in different planes, **a** microhardness distribution in the scanning plane, **b** microhardness distribution in the building plane

3.2.2 COF variations versus sliding distance

On a microscopic level, during dry sliding wear, the pin and counterface surfaces interact in a few spots (asperities or surface peaks) that are substantially smaller than the nominal surface area of the pin. Hence, the applied loads are much higher in these regions than the nominal values [68]. Consequently, the stress at the contact points exceeds the yield strength of the pin material, resulting in material removal from the surface of the Scalmalloy® pin. In other words, digging the surface of the pins due to harder asperities on the steel disc can be expected [69]. Figure 11 shows the change in COF versus sliding distance for all SN, BN, and BP samples under three applied loads, 20, 40, and 60 N. For all samples at the running-in period, the COF value increased within the first ~ 600 m, after which the COF became a plateau (steady-state).

This behavior can be related to the gradual decrease in roughness during the wear test, i.e., removing the asperity points from both contacting surfaces. A high level of frictional force is needed to overcome the material resistance (asperity yield strength) and break or deform the asperities. These small asperity contacts with different sizes and shapes make the whole actual contact areas, and then by continuing the test, these asperities become flatted or detached, and surfaces adjust to each other and cause a plateau in COF curves [40, 70].

Generally, the tiny spot welds must be broken apart at the contact surface before the two frictional pairs slide over each other [71]. It can cause oscillation in all curves shown in Fig. 11 and can be attributed to the stick–slip effect, which is more evident under 40 and 60 N load conditions.

Figure 12 a shows the average value of COF at the steady-state mode (from 600 to 2500 m), and its standard deviation was measured and shown by error bars. The mentioned sliding distance range was selected to eliminate the run-in effect on the computed data at the beginning of the wear test. It can be seen that the variation of the average COF versus applied loads is considerable for all samples. Therefore, COFs ranged from 0.45 to 0.8 for all samples in this study. Regardless of the as-built microstructure, a drastic increase was observed when the load

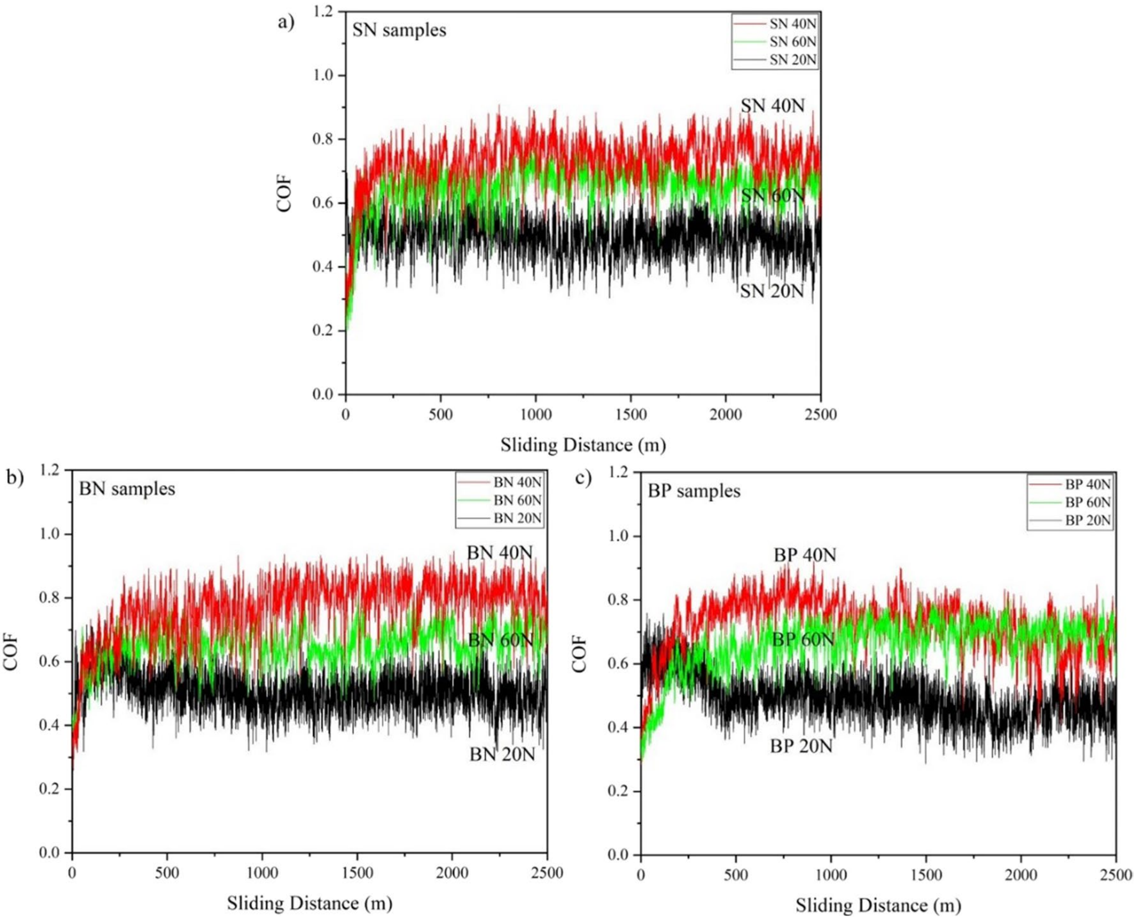

Fig. 11 Variations of COF during dry sliding wear test under different applied loads, **a** SN samples, **b** BN samples, and **c** BP samples

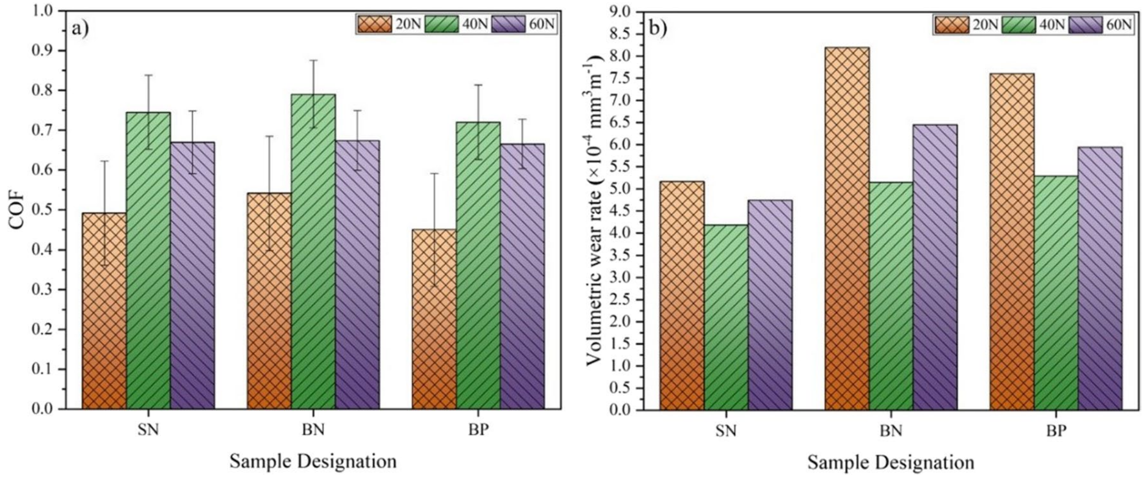

Fig. 12 Effect of different applied loads on COF variation (**a**) and volumetric wear rate values (**b**)

was increased from 20 N to higher loads (40 and 60 N). However, a slight decrease with increasing applied loads from 40 to 60 N was observed for COF. The effect of applied load variations on the average COF and volumetric wear rates for all samples are quantitatively compared and summarized in Table 3.

Notably, the average COF values drastically increased by 51, 45, and 60% in SN, BN, and BP samples by increasing the applied load from 20 to 40 N, respectively, which can be related to frictional dynamic instabilities. This sharp COF change can result from combining two main dominant mechanisms. First, there is a higher possibility of more asperities getting in contact and increasing the actual contact area by direct metal-to-metal contact (high metallic intimacy) at higher applied loads, where these large adhesion regions act as stress raisers [72]. Second, frictional heat is generated at asperities in the sliding interface, and a slight local heat expands the near-surface volume of the sample and eventually increases the COF [73].

Accordingly, it can be expected that higher COF values are obtained under higher applied loads, 40 and 60 N, compared with 20 N applied load. However, from Fig. 12 a, it can also be found that by increasing the applied loads from 40 to 60 N, COF value slightly decreased by 10, 14, and 7% in SN, BN, and BP samples, respectively, and eventually reached a constant value (~0.65) for 60 N applied load in all samples. This reduction in COF can be attributed to the combination of two main dominant mechanisms: (i) propagating stick–slip zones (slip waves) under 60 N applied load, arising from a series of breakings and adhesions of the frictional pairs at the contact points [68, 73]. (ii) Formation of oxide film between the frictional pairs, which theoretically can result from the temperature rises due to higher frictional heat at the highest applied load (60 N), regardless of the as-built microstructure, which in turn causes a slight reduction in COF value [44, 74].

Therefore, the lowest COF at the lowest applied load (20 N) in this study can be attributed to the combination of the two main dominant mechanisms: (i) formation of oxide film due to the nature of the aluminum alloy, (ii) fewer asperities contact leading to separation of two metal surfaces and a smaller actual contact surface. Although oxide film still existed at high applied loads of 40 and 60 N, the film could be broken and hence was a less effective mechanism in reducing COF. Therefore, a significant increase in COF values from 20 N applied loads to 40 and 60 N applied loads was revealed but slightly reduced from 40 to 60 N [75]. No dependency of COF to as-built microstructure was observed under 60 N applied load so all samples showed a constant COF.

Under the 20 and 40 N applied loads, slightly higher COF of BN samples were due to their columnar morphology and coarser grain size (Fig. 8b), compared to SN samples with much finer grain size (Fig. 7b). This difference

Table 3 Quantitative comparison of the applied load variations on COF and volumetric wear rate

Samples	COF (%)			Volumetric wear rate (%)		
	20 to 40 N	40 to 60 N	20 to 60 N	20 to 40 N	40 to 60 N	20 to 60 N
SN	51(+)	10(−)	36(+)	19(−)	13(+)	8(−)
BN	45(+)	14(−)	24(+)	37(−)	25(+)	21(−)

Sign(+), means increased percentage and sign(−), means decreased percentage can be attributed to grain boundary lubrication and higher hardness for finer grains. The refined grains in SN samples showed a higher wear resistance and lowered COF [76, 77]. Although the BP sample possesses a columnar and coarser grain size than the SN sample, it offers slightly lower COF, especially under the 20 N applied load. It will be addressed in the following section. Boundary lubrication is a mechanism where a thin lubricant film separates the two surfaces in relative motion. This lubricant film reduces the direct contact between the surfaces, thereby minimizing friction and wear. The finer grain size observed in the SN samples contributes to a practical boundary lubrication effect. The presence of finer grains aids in smoother surface contact, reducing frictional forces and wear rates. Additionally, forming an oxide film reduces the COF by acting as a boundary lubricant, preventing direct metal-to-metal contact [78, 79]. Understanding the dynamics of boundary lubrication in the context of the material's microstructure and the applied loads can provide valuable insights into optimizing the wear resistance of L-PBF Scalmalloy®.

3.2.3 Correlation of normal applied load and as-built microstructure with wear anisotropic behavior

The lower wear resistance in both BN and BP samples than the SN samples is shown in Fig. 12 b. The higher wear resistance in the SN samples can be attributed to their as-built microstructural features and microhardness that degrade the material by plastic deformation and detachment of materials from the surface of the samples. The SN samples show much less dependency on the applied loads than BN and BP samples, which can be attributed to the finer and uniform microstructure and grain boundary strengthening observed in SN samples. Therefore, three dominant reasons in combination can be considered for this anisotropic wear resistance between scanning and building planes.

(i) Due to the existing much coarser columnar grains and inhomogeneous microstructure in the building planes (BN and BP samples) (Fig. 8b), and their lower microhardness values (Fig. 10b), the resistance of the material against plastic deformation and detachment is much lower, and coarser debris can be expected as well (Fig. 19a,b). (ii) Higher possibility of the presence of internal L-PBF process-induced defects (metallurgical porosities, LOF, and unmelted powders) in the building plane (Fig. 5), which were susceptible local areas for material weaknesses and reduced the bonding between molten pools, facilitating the crack initiation-propagation at the contact surface during the dry sliding wear test in the building plane [63]. Moreover, porosities in the wear surface increase the wear rate by reducing the surface contact area against the abrasive surface [80]. Likely, the existence of a relatively low amount of surface porosities in the scanning plane (SN samples) [81], compared to the building plane, results in a lower chance of crack formation when loads are applied, thus positively improving its wear resistance [74, 82]. Notably, the appearance of higher strain localization of columnar grains inside the MPs and highly strained regions around the internal defects can be considered a material weakness of the building plane during deformation [83]. (iii) The hatching distance parameter (h), one of the most critical L-PBF process parameters, can generate many interaction points between adjacent laser tracks and their resulting MPBs in the building plane (Fig. 6b). These critical points can act as crack initiation sites and weaken the material against normally applied loads [84]. Thus, they can promote crack initiation and facilitate material detachment and plastic deformation during the dry sliding wear test in the building plane.

The BN samples have higher COF than BP samples (under 20 and 40 N applied loads), showing slightly higher wear rate values. It can be realized that conducting the wear test parallel and perpendicular to the columnar grains offers a somewhat different wear value. It can be concluded that when columnar grains were exposed to the wear in BN samples, the loads were exerted on the short axis of columnar grains, while in BP samples, the long axis of columnar grains was subjected to the wear test. Notably, columnar grains in the building plane grow toward the maximum thermal gradient. Considering the 67° rotation between the layers during the L-PBF process, complicated thermal history is expected across the sample, resulting in a tilted direction of solidification front along the sample's building direction (*Z*) [37]. Thus, it cannot be expected that all columnar grains were precisely perpendicular to the BN samples' wear direction. Accordingly, the wear rates of BN and BP samples are slightly different, especially under 40 and 60 N applied loads. Thus, higher wear rate differences can be seen under the lowest applied load, i.e., 20N, than 40 and 60 N, due to higher compressive stress under higher applied loads. These results indicate that, under a lower applied load (20 N), the as-built microstructural features in the building and scanning planes strongly influenced the material's wear resistance and COF. On the other hand, under higher applied loads (40 and 60 N), the effect of external loads outweighs the as-built microstructural features in terms of wear rate and COF. The wear rate differences observed under varying applied loads, particularly the distinct prominence of these differences under the lowest applied load (20 N) compared to 40 and 60 N, can be further explained by the influence of compressive stress. At a lower applied load, the inherent microstructural features in the building and scanning planes significantly impact the material's wear resistance and coefficient of friction (COF). However, with increased applied loads (40 and 60 N), the effect of external forces becomes more predominant, leading to a relatively diminished influence of the as-built microstructural characteristics on the wear rate and COF. This phenomenon highlights the complex interplay between applied loads and the intrinsic properties of the material, emphasizing the critical role of both factors in the wear behavior observed.

3.2.4 Correlation of worn surface and normal applied load with the wear rate and its mechanisms

To further investigate the wear behavior of L-PBF Scalmalloy® and its features from a microstructural point of view, the corresponding worn surfaces were characterized by FE-SEM, as portrayed in Fig. 13 (a–i). For SN samples Fig. 13 (a–c), clearer, smoother, and less erratic worn surfaces were observed than other wear test conditions noticed for the BN and BP samples, which can be considered evidence for higher wear resistance of SN samples. The variations in wear resistance are associated with anisotropy in the samples.

Also, the volumetric wear rate of all samples versus the applied loads is shown in Fig. 12 b. The wear volume due to fragments from a portion of asperities during sliding can be determined, and wear occurs due to interaction between asperities. Under the 20 N applied load, the highest wear rate between all three sample groups was calculated. Likely, under the 20 N applied load conditions, the abrasive wear

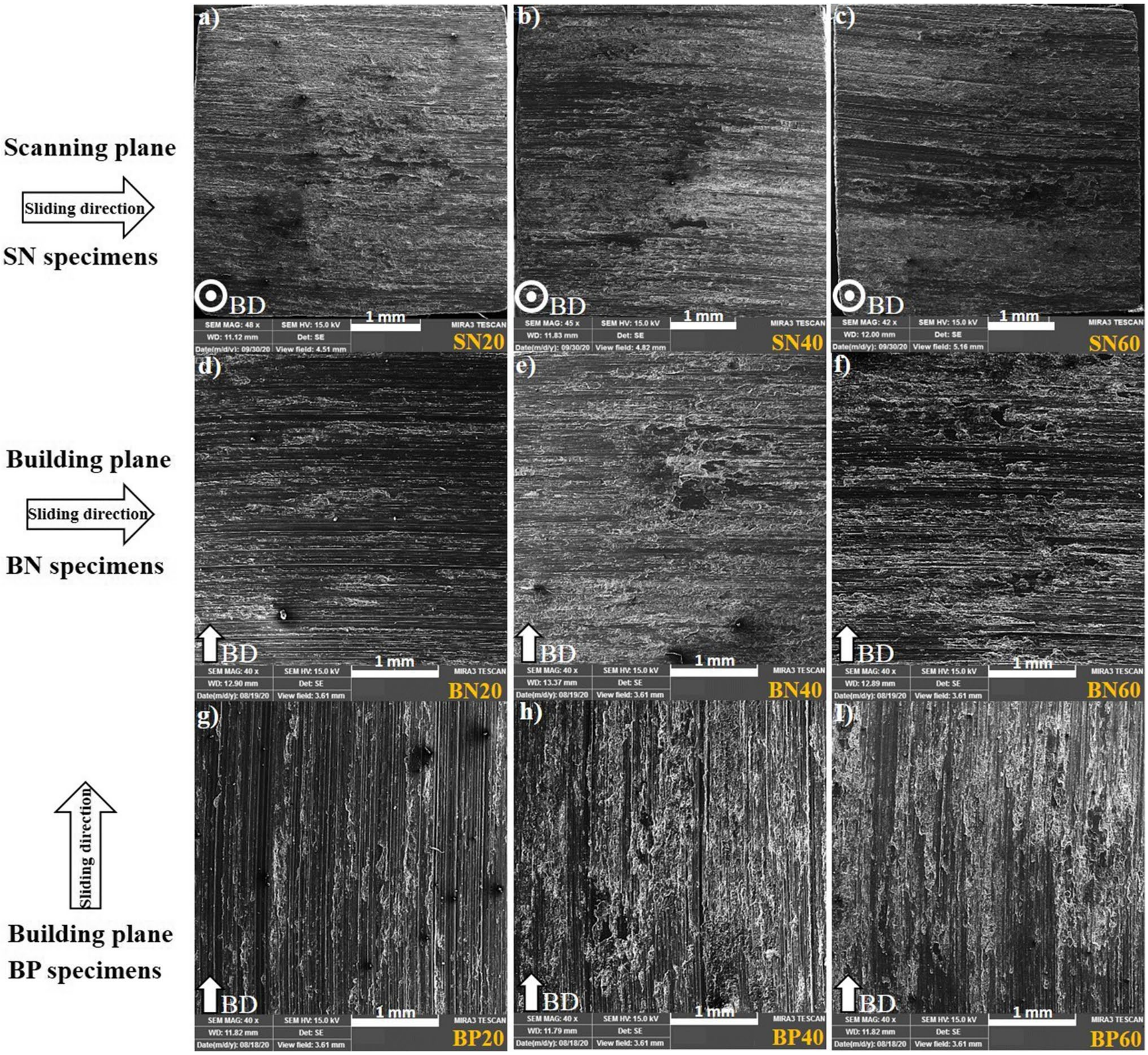

Fig. 13 Comparative FE-SEM investigation of all worn surfaces. **a**, **b**, and **c** show the worn surfaces of SN samples; d, e, and f show the worn surfaces of BN samples; **g**, **h**, and **i** show the worn surfaces of BP samples at 20 N, 40 N, and 60 N applied loads, respectively

mechanism via ploughing of the surface by hard asperities was more dominant. Therefore, material removal from the surface could be expected by creating long parallel deep grooves and delaminations, as shown in Fig. 13 d, and Fig. 14 a [65, 85]. According to Fig. 12 b, applied loads play a significant role in the wear rate values in all samples. Although COF drastically increased by increasing applied loads from 20 to 40 N, the volumetric wear rate decreased by 19%, 37%, and 30% for SN, BN, and BP, respectively (steeper in the BP and BN samples than in the SN samples). This decrease in wear rate is likely due to prevailing plastic deformation and flattening of the asperities in the adhesive wear mechanism under 40 and 60 N applied loads. In addition, due to more compressive stresses, the wear rate in both scanning and building planes under high applied loads (40 and 60 N) is much lower than the 20 N applied load. Nevertheless, the wear anisotropic behavior is more prominent under the low applied load of 20 N.

Figure 13 d shows the worn surface belonging to the highest wear rate in this study, i.e., the BN20 sample. It reveals a remarkable difference in the wear characteristic compared to the BN40 sample (Fig. 13e). It can be seen that under 40 N applied load, a smoother and clearer surface with fewer long grooves was generated, which can be attributed to the flattening of the asperities in the actual contact area. Asperities contact points under the 20 N applied load were smaller and fewer than 40 N, and 60 N applied loads. On the other hand, the material yield strength, in this case, is scale-dependent; therefore, the strength of the material is much higher in asperity contact than the bulk material [86, 87]. Thus, under the 40 N applied load, much more high-strength asperity contacts were generated, and a higher rate of work hardening during sliding could be expected; hence, more resistance to material detachment and wear could be expected.

Consequently, a drastic decrease into a much lower wear rate in the 4 0N applied load, compared to 20 N, resulted in all samples (especially for BN and BP samples). However, increasing the applied load from 40 to 60N slightly increased the wear rate by 13%, 25%, and 12% in SN, BN, and BP samples, respectively. This change can be related to the 60 N applied load exceeding the strength of the asperities and reducing the continuity of the oxide film layer during sliding. Accordingly, no direct correlation between COF and wear rate was revealed; hence, wear could only be related to a fraction of the energy used in the wear process [73], a finding which will be discussed meticulously along with the following microstructural analysis. The significant effect of different as-built microstructures along the scanning and building planes on dominant wear mechanisms and scars under the constant applied load of 20 N is depicted in Fig. 14 a and b. A higher magnification of the worn surface corresponding to the BN20 sample (Fig. 13d) is shown in Fig. 14 a. It can be noticed that the worn surface of the sample with the highest wear rate, i.e., ~ 8.2 mm^3/m is featured by many long parallel deep grooves, small debris, and delaminations. The lowest wear rate, i.e., ~ 4.2 mm^3/m under the same 20 N applied load, belonged to the SN20 sample (Fig. 13a), shown in higher magnification in Fig. 14b.

Figure 14 a shows the BN20 worn surface consisting of small yellow circles, which indicate additional wear debris

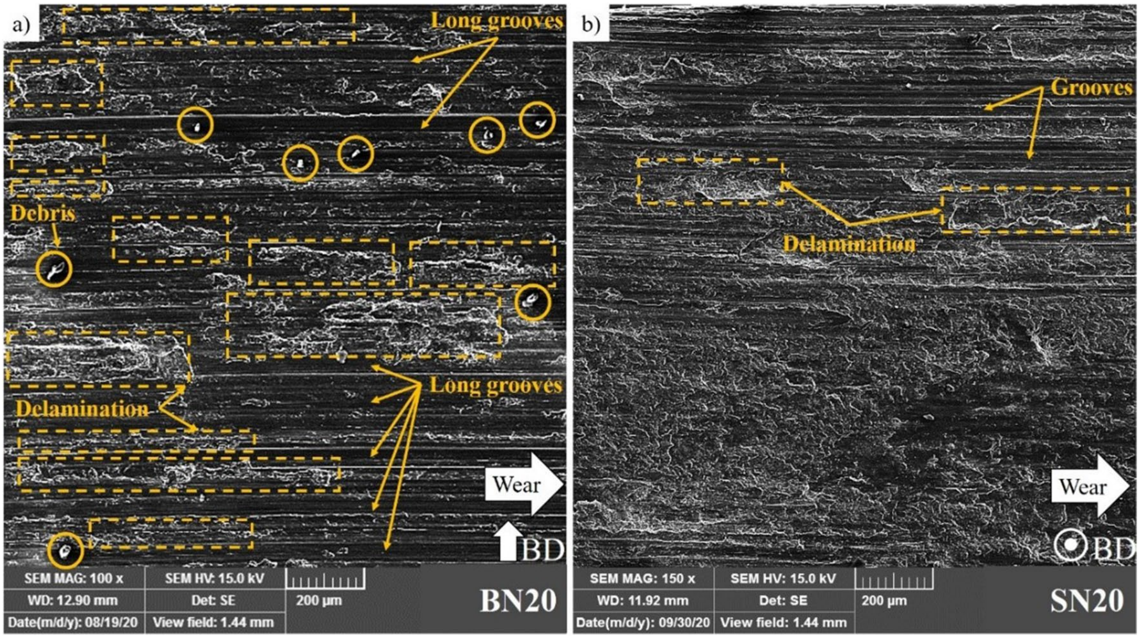

Fig. 14 The worn surface at the same applied load 20 N, **a** BN20 sample at 100 × magnification, **b** SN20 sample at 150 × magnification

corresponding to different internal defects and oxidation in the building plane during sliding. Also, arrows show the long parallel grooves running in the sliding direction along the whole surface of the sample due to hard protrusions on the wearing steel disc. Furthermore, dashed boxes reveal delaminations and severely detached material. In contrast, in Fig. 14 b, the smoother worn surface, delaminations, and much fewer parallel grooves of the SN20 sample can be attributed to the higher wear resistance along the scanning plane with higher microhardness. In the bottom area of Fig. 14 b, the plastic deformation of the material by flattening and smoothing the asperities can be seen.

Further microstructural investigations from the worn surface of the BN20 sample in higher magnification are shown in Fig. 15. The figure features with abrasive wear signs such as long parallel grooves, delaminations, ploughing, cutting, and debris similar to the items marked in Fig. 14 a. Also, the removed material can be noticed at the top of Fig. 15 b. In contrast, plastically deformed areas are shown at the bottom. Moreover, traction within the contact area might result in surface features and cracks in the plastically deformed area perpendicular and parallel to the sliding wear direction, as shown in Fig. 15 c. The appearance of very high and repeated surface stresses during the sliding test leads to a surface fatigue wear mechanism, where voids are generated at the sub-surface inducing crack formation in three steps. These steps include crack initiation, growth, and eventually, the formation of large fragments of material from the surface, Fig. 15 b and d. The propagation of the cracks into the heavily deformed layer can lead to delamination and debris formation [88–90]. Accordingly, under the constant applied load of 20 N, the surface fatigue wear and abrasion mechanisms are more dominant, especially for BN and BP samples, which are commensurate with their higher wear rates measured.

Figure 16 shows the highest applied load (60 N) effect on the worn surface and wear mechanism for the BP60 sample. At the contact surface, under higher applied loads, plastic shearing of the softer asperities (pin) leads to adhesion between asperities of the frictional pairs when they are loaded against each other. Due to plastic flow, nucleation and propagation of sub-surface cracks lead to platelet-like wear particles before extending out to the free surface, promoting delamination and material shell-off [74]. A mechanically mixed layer (MML) containing Al–Fe–Cr–O compounds that adhere to the pin was formed during sliding; further sliding, this layer gets separated from the pin surface due to delamination, as shown in region G in Fig. 16 (a), [91], and these separate layers by delamination promote the adhesive wear mechanisms.

Figure 16 (b, c) shows differences between the EDS analysis of G and H regions regarding O, Fe, and Cr contents. Higher Fe, Cr, and O amounts in region H can be attributed to MML formation.

The possibility of the three-body abrasion and oxidative wear mechanisms is explored in the following paragraphs. Figure 17 shows the back-scattered electron (BSE) microscopy and SEM–EDS analysis from the worn surface of the BP60 sample at a higher magnification. The existence of white particles A (13.5 wt% of C, 36.5 wt% of Cr, and 44.0 wt% of Fe) and C (12 wt% of C, 26 wt% of Cr, and 55 wt% of Fe) indicates a material transfer from counter material (AISI 52100 bearing steel), used as a wearing disc, which proves the adhesive wear mode was the dominant wear mechanism under the 60 N applied load conditions. Moreover, Fig. 17 b shows a bulk-EDS from the worn surface of the BP60 sample, in which a high amount of Fe (~ 23 wt%), Cr (~ 2.7 wt%), and oxygen (~ 32 wt%) throughout the Al matrix can be seen. In addition, more local analysis from region B (severely plastically deformed region or MML) in Fig. 17 d and region D (inside the delamination zone). Figure 17 f proves the existence of a high amount of oxygen and Fe, C, and Cr elements from the counterface. The presence of carbon can explain the slight decrease of (7%) COF when the load increased from 40 to 60 N. In addition, a higher amount of Fe and Cr was observed in region B than in region D, which can propose the MML formation during the sliding. However, it is noteworthy that a much lower amount of Fe and Cr elements was observed under the 20 N applied load conditions, while no carbon was detected (Fig. 15c).

For all samples, Fig. 18 shows the weight percent of Al, Fe, O, and Cr elements of the worn surface. It is observed that under 40 and 60 N applied loads, the Fe and Cr concentrations being (20–24 wt%) and (2–4 wt%), respectively, are higher than in the 20 N applied load. This evidence proves that when applied loads reach higher values, some main alloying elements from the counterface (wearing disc) can transfer and enter the sample, promoting the adhesive wear mechanism [68]. However, a relatively constant and high oxygen (32–35 wt%) level was shown that an oxide layer mostly covered the worn surface. Oxide can be generated between solid surfaces of the two frictional pairs due to the oxidative wear mechanism, especially under a high sliding distance designated in this study (2500 m) [64]. It can be concluded that the growth of oxide layers and adhesive transfer of material between the sample and wearing disc were the main dominant wear mechanisms under the 40 and 60 N applied loads regardless of the as-built microstructure [46]. Adhesive wear mechanisms limited the amount of wear under the 40 and 60 N applied load compared to the abrasive wear mechanisms observed under the 20 N applied load [92]. Moreover, it can be expected that during the sliding under 40 and 60 N applied loads, the formation of stable and compacted layers (MMLs) was promoted and led to a

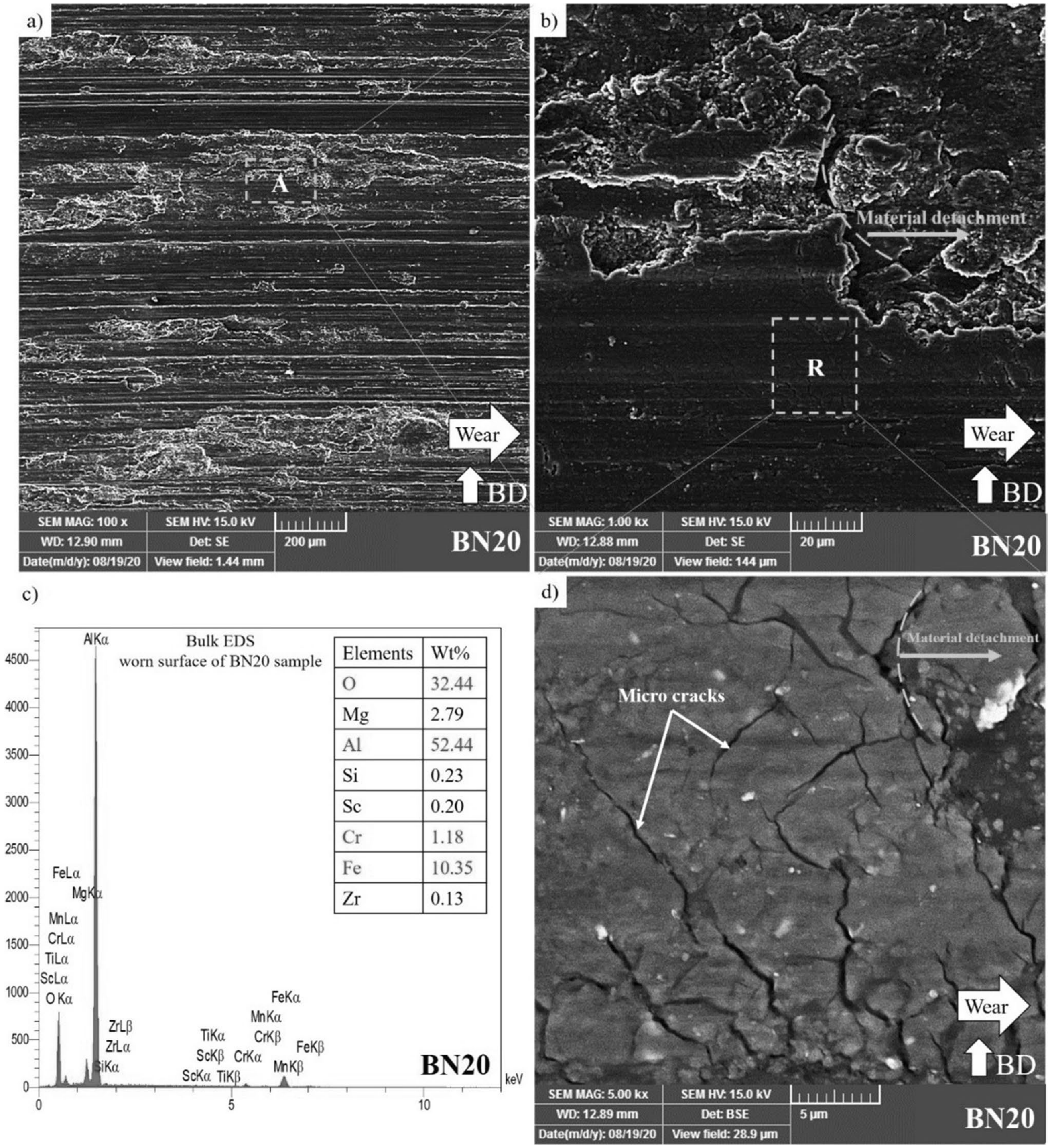

Elements	Wt%
O	32.44
Mg	2.79
Al	52.44
Si	0.23
Sc	0.20
Cr	1.18
Fe	10.35
Zr	0.13

Fig. 15 Abrasion wear mechanism under the applied load 20 N. a Secondary electron microscopy from the worn surface of the BN20 sample, b higher magnification of region A in (a), c bulk-EDS analysis from the whole worn surface (a), d higher magnification of region R in (b)

remarkable decrease in wear rate compared to 20 N applied load [91, 93].

Notably, the change in the total weight percentage of the Al element on the worn surface of each sample is not solely caused by changes in the concentration of Fe and Cr. As mentioned earlier, the presence of an oxide layer on the worn surface primarily contributes to the alteration in the weight percentage of Al. The higher concentrations of Fe and Cr under 40 and 60 N applied loads indicate the transfer of these elements from the wearing disc to the sample,

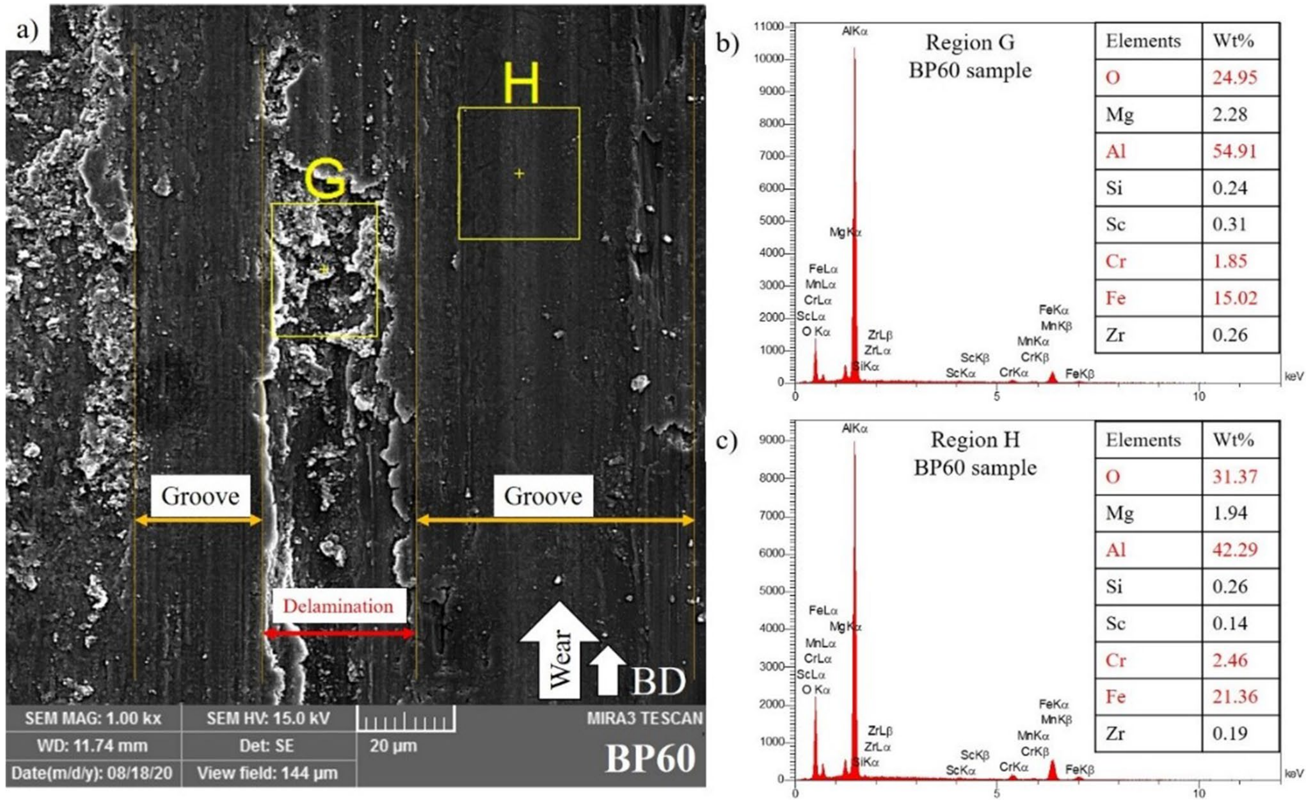

Elements	Wt%
O	24.95
Mg	2.28
Al	54.91
Si	0.24
Sc	0.31
Cr	1.85
Fe	15.02
Zr	0.26

Elements	Wt%
O	31.37
Mg	1.94
Al	42.29
Si	0.26
Sc	0.14
Cr	2.46
Fe	21.36
Zr	0.19

Fig. 16 (a) The worn surface of the BP60 sample, (b) the EDS analysis from inside the delamination region G in (a), (c) the EDS analysis from inside the groove region H in (a)

promoting the adhesive wear mechanism. Additionally, the constant and high oxygen level suggests the predominance of an oxide layer covering the worn surface, generated due to the oxidative wear mechanism. This oxide layer formation between the two frictional pairs contributes significantly to the changes in the weight percentage of Al. The growth of oxide layers and the adhesive transfer of material between the sample and the wearing disc are the main wear mechanisms under the 40 and 60 N applied loads, leading to a decrease in the wear rate compared to the 20 N applied load. Furthermore, the formation of stable and compacted layers during sliding, known as mechanically mixed layers (MMLs), contributes to the overall changes observed in the wear behavior of the samples.

3.2.5 Correlation of wear products with wear mechanisms

Figure 19 (a, b, and c) show different debris sizes, being coarse (plate-like flakes) for BN samples (a), moderate (mixture of fine particles and plate-like flakes) for BP samples (b), and fine to ultra-fine for SN samples (c). This size difference can explain the higher wear resistance of SN samples. Fine and ultra-fine debris in SN samples can easily fill the vacant junctions of the contact surface and promote smoothening of worn surfaces (Fig. 13 (a–c)). The material taken from the surface may be readily smeared out and dispersed across the counter surface, acting as a solid lubricant during dry sliding [94].

However, in the BN samples with a high amount of long columnar grains, coarser debris detached and accumulated along the contact surface, adhering more to the softer material during the sliding distance, increasing the wear rate [44]. The flaky morphology of debris represents the process of delamination along with the BN and BP samples. According to all the mentioned surface damages analysis, the debris pull-out from the tips of the asperities was expected when adhesive forces were combined with plastically flowing material. It can be seen that the formation of coarse debris from the BN sample is predominant, which can be attributed to the presence of long columnar grains as distinctive microstructural features of the building plain (Fig. 8b). However, fine and ultra-fine debris for SN samples were related to the higher microhardness and refined grains and their relatively uniform equiaxed as-built microstructure of SN samples (Fig. 7b) [72].

On the other hand, a combination of both the dominant discussed debris was formed for BP samples (Fig. 19b). More EDS analysis of the SN debris is shown in Fig. 19

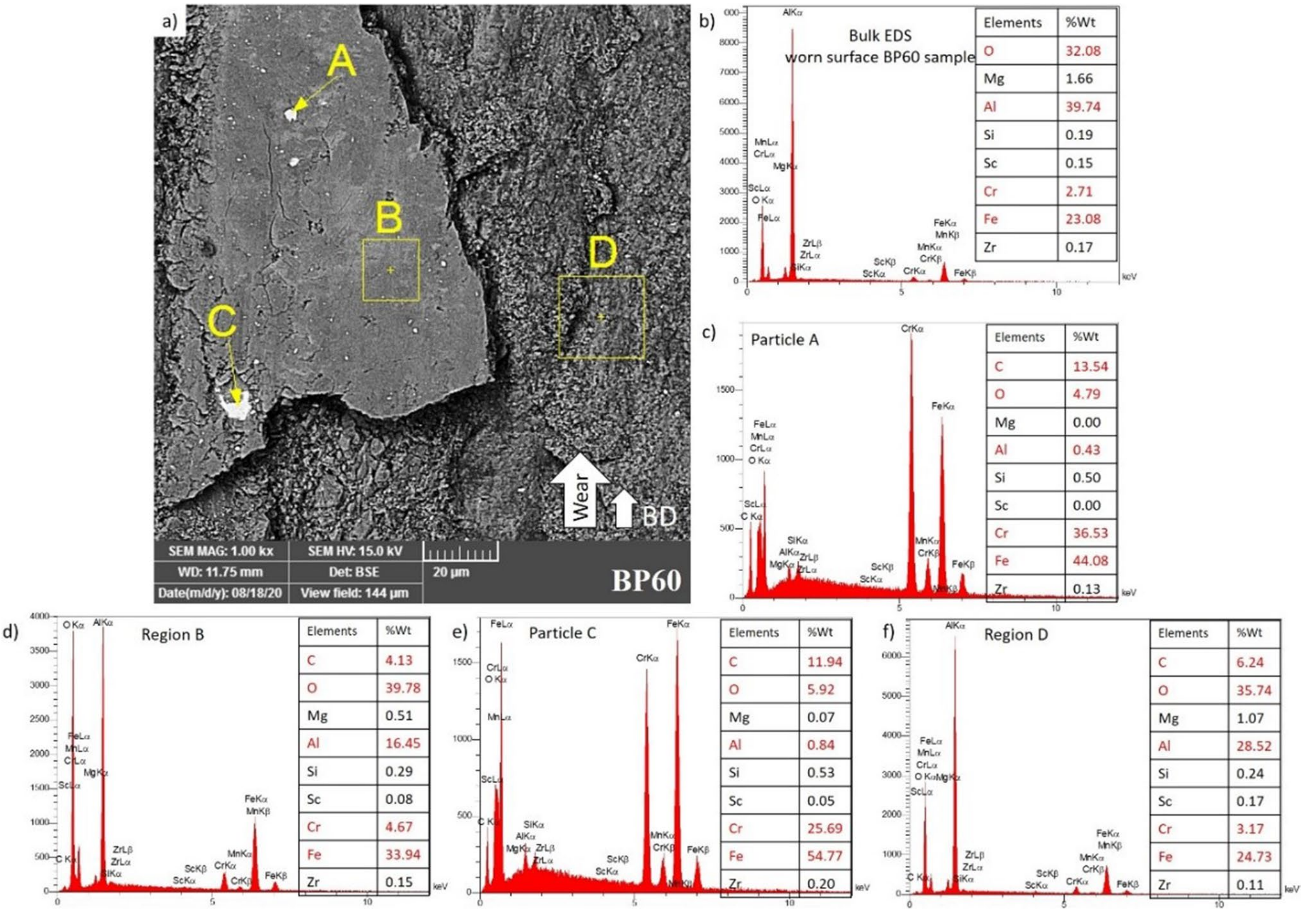

b) Bulk EDS worn surface BP60 sample

Elements	%Wt
O	32.08
Mg	1.66
Al	39.74
Si	0.19
Sc	0.15
Cr	2.71
Fe	23.08
Zr	0.17

c) Particle A

Elements	%Wt
C	13.54
O	4.79
Mg	0.00
Al	0.43
Si	0.50
Sc	0.00
Cr	36.53
Fe	44.08
Zr	0.13

d) Region B

Elements	%Wt
C	4.13
O	39.78
Mg	0.51
Al	16.45
Si	0.29
Sc	0.08
Cr	4.67
Fe	33.94
Zr	0.15

e) Particle C

Elements	%Wt
C	11.94
O	5.92
Mg	0.07
Al	0.84
Si	0.53
Sc	0.05
Cr	25.69
Fe	54.77
Zr	0.20

f) Region D

Elements	%Wt
C	6.24
O	35.74
Mg	1.07
Al	28.52
Si	0.24
Sc	0.17
Cr	3.17
Fe	24.73
Zr	0.11

Fig. 17 Material transfer under the applied load 60 N. (a) Back-scattered electron microscopy from the worn surface of BP60 sample, (b) bulk-EDS analysis from the whole worn surface, (c) point-EDS analysis from particle A, (d) EDS analysis from region B, (e) point-EDS analysis from particle C, and (f) EDS analysis from region D

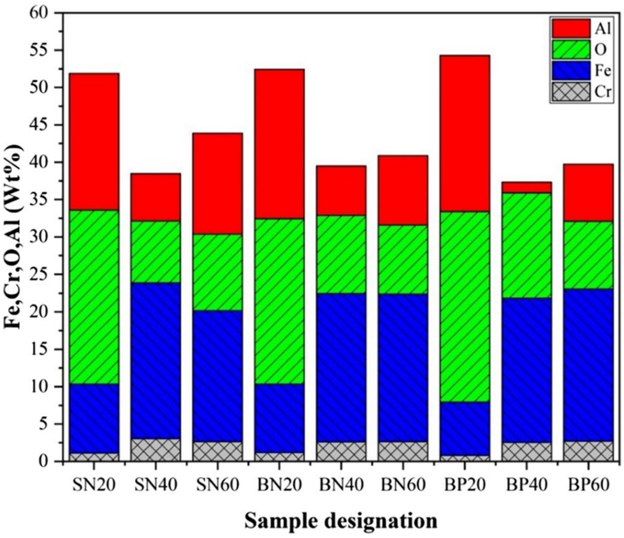

Fig. 18 The total weight percent of Fe, Cr, O, and Al elements in the worn surface of all samples

(d–f); it can be seen that those particles can consist of a high level of oxygen (~40 wt%) (Fig. 19d, e) due to oxidation during the sliding. In contrast, some particles come from the counterface material having a high amount of Fe and Cr elements (Fig. 19f). Due to the micro-cutting action of the countersurface, oxide layers might build over time and readily break down into hard abrasive oxide particles [95].

Thus, from the debris analysis in Fig. 19 (a, b, c, d, and f) and the appearance of high amounts of Fe and Cr elements (Fig. 18), it can be concluded that the three-body abrasion mechanism was also possible, regardless of the as-built microstructure. It can be attributed to hard particles enriched by Fe and Cr elements (especially under 40 and 60 N applied loads). Moreover, fragmentation of oxide film layers (especially under 20 N applied load) could promote the three-body abrasion wear mechanism and generate deep groove scratches parallel to the wear direction (Fig. 13 and 16). Notably, oxides act as abrasive particles, contributing to abrasive wear.

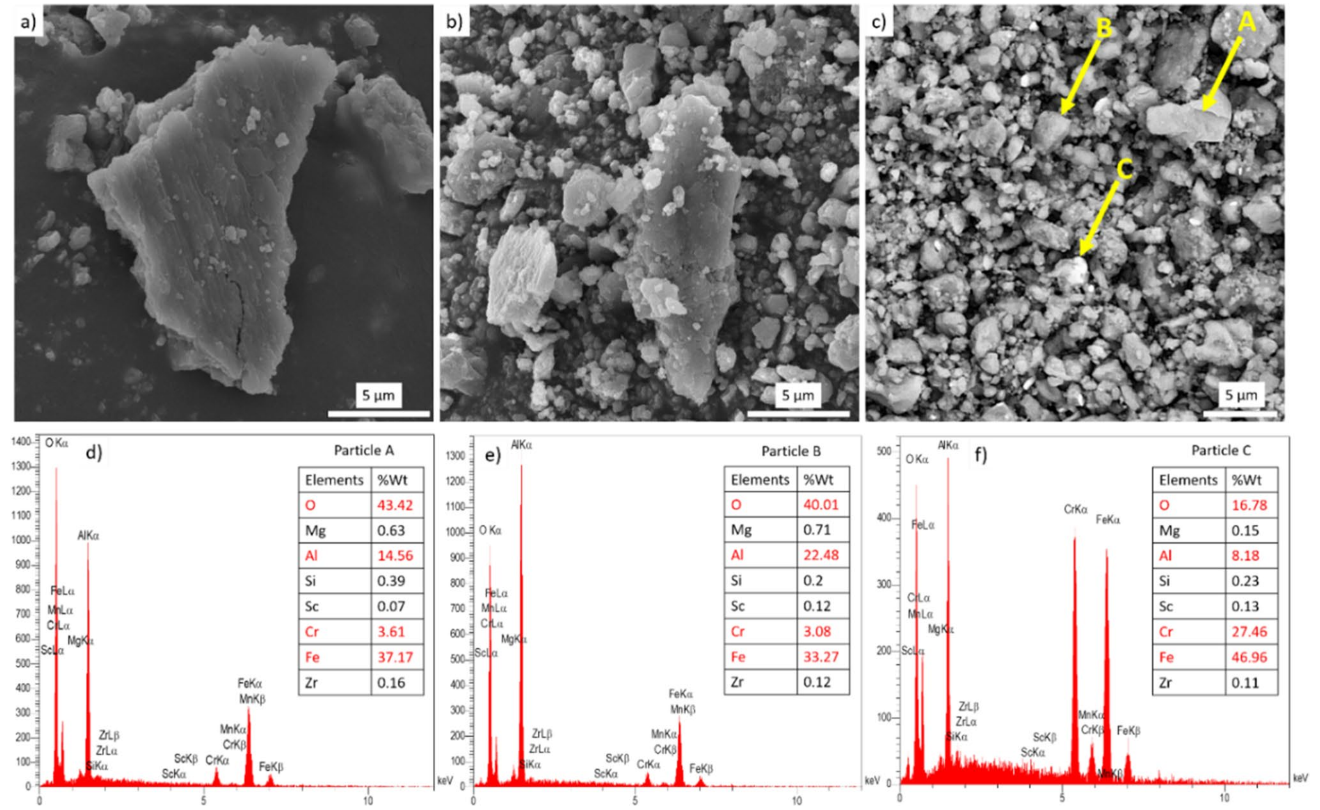

Particle A

Elements	%Wt
O	43.42
Mg	0.63
Al	14.56
Si	0.39
Sc	0.07
Cr	3.61
Fe	37.17
Zr	0.16

Particle B

Elements	%Wt
O	40.01
Mg	0.71
Al	22.48
Si	0.2
Sc	0.12
Cr	3.08
Fe	33.27
Zr	0.12

Particle C

Elements	%Wt
O	16.78
Mg	0.15
Al	8.18
Si	0.23
Sc	0.13
Cr	27.46
Fe	46.96
Zr	0.11

Fig. 19 Different sizes of debris for BN (a), BP (b), SN (c) samples, and EDS analysis (d, e, and f) of A, B, and C particles in (c), respectively

In conclusion, the sliding wear test demonstrated the operation of multiple wear mechanisms, each contributing differently depending on the sliding conditions [96]. In other words, a combination of adhesive and abrasive mechanisms, delamination, surface cracking, and oxidation was observed. Therefore, different values were measured for the wear rate depending on which wear mechanisms were predominant. Figure 20 represents the schematic of the dominant wear damage and material detachment mechanisms from a microstructural viewpoint to display the wear characteristics in this study. Figure 20 (a, b, and c) show BN, BP, and SN samples, respectively. In Fig. 20 (a and b), 1 indicates a columnar grain inside a MP; 2, shows ultra-fine equiaxed grains along the MPBs; 3, indicates that L-PBF process induced-unmelted spherical powders can act as some weakness sites of the material under the wear test; 4, shows plastically deformed area of material before detachment from the surface; 5, is indicative of crack initiation and propagation; 6, marks a wear product (debris); 7, shows scars or delaminations (due to detached material); and 8, marks the end of a long groove. In Fig. 20 (c), 1 shows refined equiaxed grains inside the laser scan track, and 2 shows ultra-fine grains at the laser scan track boundary.

4 Conclusions

Scalmalloy® samples were successfully produced using optimum L-PBF process parameters. A comparative study on the effect of different as-built microstructures on the tribological performance of the alloy was conducted under different contact loads. The key concluding remarks of this study can be summarized as follows:

1. The microstructural analysis of L-PBF Scalmalloy® showcased diverse defects, including internal gas porosities, lack of fusion porosities, as well as columnar grains and ultra-fine equiaxed grains. Chemical element distribution along the molten pool boundaries was evident, and the XRD analysis confirmed the prevalence of the α-Al (fcc) phase.
2. Vickers microhardness tests on the scanning and building planes of Scalmalloy® highlight the impact of the as-built microstructure. The scanning plane exhibits higher and more uniform microhardness (95.2 HV on average) than the building plane (89.5 HV on average), attributed to the finer microstructure and increased dis-

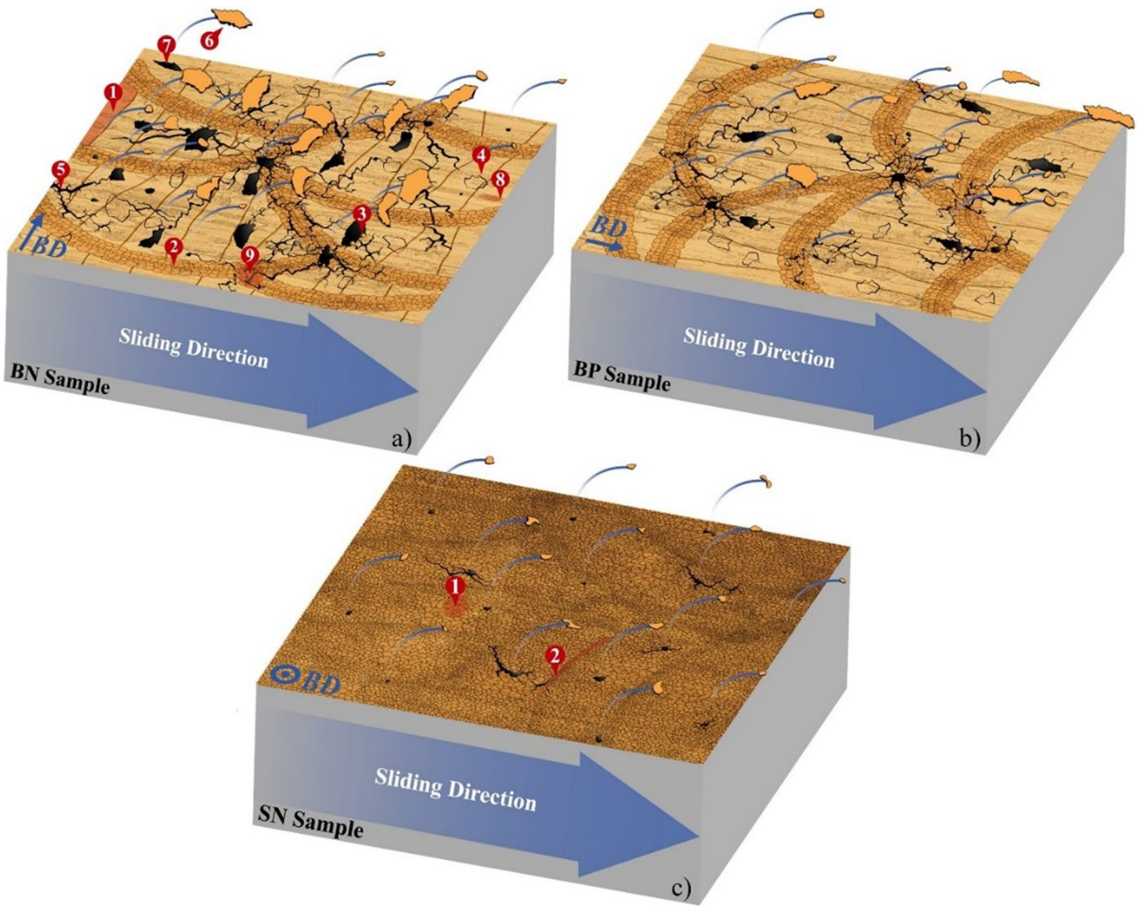

Fig. 20 Schematic of the effect of as-built microstructure on wear mechanisms of L-PBF samples. **a** A BN sample, **b** a BP sample, and **c** an SN sample

location density. This suggests higher wear resistance in the scanning plane.

3. The coefficient of friction during the wear test initially increased as the surfaces interacted, followed by a plateau. This pattern indicates the removal of surface asperities and the adjustment of surfaces to each other. The stick–slip effect was observed under higher applied loads, causing oscillation in the COF curves.
4. The coefficient of friction varied with applied loads, increasing sharply from 20 to 40 N due to increased contact and frictional heat, with a slight decrease from 40 to 60 N. The lowest COF was at 20 N, attributed to oxide film formation and fewer contacts. No significant COF dependency on the microstructure was observed at 60 N, indicating a constant COF for all samples. The BN sample had slightly higher COF due to its columnar morphology and coarser grain size compared to the SN sample.
5. Microstructural differences, internal defects, and process parameters influence the anisotropic wear behavior. The building plane samples showed lower wear resistance due to their coarser microstructure and the presence of internal defects, while the scanning plane samples exhibited better resistance owing to their finer and more uniform microstructure. The compressive stress influenced the varying wear rates under different loads, indicating the complex interplay between applied loads and material properties in determining wear behavior.
6. The worn surface analysis indicates distinct wear characteristics. Scanning plane (SN) samples exhibit smoother surfaces, suggesting higher wear resistance compared to building plane (BN and BP) samples. Under lower applied loads, abrasive wear dominates, while higher loads lead to plastic deformation and reduced wear rates. Microstructural differences, including internal defects and varying grain sizes, significantly affect wear behavior. Adhesive wear mechanisms, such as material transfer and oxide layer formation, prevail under higher loads, minimizing wear compared to abrasive mechanisms observed under lower loads.
7. The study identifies various wear mechanisms during the sliding wear test, with SN samples exhibiting

finer debris due to their higher microhardness. Coarser debris in BN samples is attributed to their long columnar grains. Fe and Cr elements suggest the possibility of a three-body abrasion mechanism. The combined action of adhesive and abrasive wear, along with delamination, surface cracking, and oxidation, influences the observed wear rates.

8. This research study unveils the anisotropic wear properties of as-built L-PBF Scalmalloy® resulting from microstructural differences. This paper can draw the attention of AM designers to exploit an appropriate DfAM approach to achieve better tribological performance for Scalmalloy® components from industrial frictional pair standpoints. The authors suggest more research topics for future studies, including evaluating the effect of additional lubrication, post-heat treatment cycles, surface roughness, and different sliding velocities on the tribological performance of additively manufactured Scalmalloy® samples.

Acknowledgements The authors would like to thank Dr. Jukka Pakkanen for supplying the powder and L-PBF specimens.

Author contribution A. A. and A. S. conceived and designed the experiment. A. A. and S. A. F performed the characterizations and collected the data. All the authors analyzed and interpreted the data. A. A. and M. S. S. wrote and revised the first draft of the manuscript. L. I., A.S., and M. S. S supervised the work, revised the manuscript, and approved the final version to be submitted.

Funding Open access funding provided by Politecnico di Torino within the CRUI-CARE Agreement.

Data availability The datasets generated during and/or analyzed during the current study are available from the corresponding author on reasonable request.

Code availability Not applicable.

Declarations

Ethics approval This chapter does not contain any studies with human participants or animals performed by any of the authors. The authors acknowledge the work is original and all the relevant texts from the literature have been properly cited.

Consent to participate The authors agree to the authorship order.

Consent for publication All the authors have read and agreed to the published version of the manuscript.

Conflict of interest The authors declare no competing interests.

References

1. Galati M, Defanti S, Saboori A, Rizza G, Tognoli E, Vincenzi N, Gatto A, Iuliano L (2022) An investigation on the processing conditions of Ti-6Al-2Sn-4Zr-2Mo by electron beam powder bed fusion: microstructure, defect distribution, mechanical properties and dimensional accuracy. Addit Manuf 50:102564. https://doi.org/10.1016/j.addma.2021.102564
2. Saboori A, Gallo D, Biamino S, Fino P, Lombardi M (2017) An overview of additive manufacturing of titanium components by directed energy deposition: microstructure and mechanical properties. Appl Sci 7:883. https://doi.org/10.3390/app7090883
3. Emmelmann C, Kranz J, Herzog D, Wycisk E (2013) Laser additive manufacturing of metals. In: Schmidt V, Belegratis M (eds) Laser technology in biomimetic. Springer, Berlin, Heidelberg, pp 143–162. https://doi.org/10.1007/978-3-642-41341-4_6
4. Roccetticampagnoli M, Galati M, Saboori A (2021) On the processability of copper components via powder-based additive manufacturing processes: potentials, challenges and feasible solutions. J Manuf Process 72:320–337. https://doi.org/10.1016/j.jmapro.2021.10.038
5. Aversa A, Saboori A, Librera E, De Chirico M, Biamino S, Lombardi M, Fino P (2020) The role of directed energy deposition atmosphere mode on the microstructure and mechanical properties of 316L samples. Addit Manuf 34:101274. https://doi.org/10.1016/j.addma.2020.101274
6. Mosallanejad MH, Niroumand B, Aversa A, Manfredi D, Saboori A (2021) Laser powder bed fusion in-situ alloying of Ti-5%Cu alloy: process-structure relationships. J Alloys Compd 857:157558. https://doi.org/10.1016/j.jallcom.2020.157558
7. Saboori A, Abdi A, Fatemi SA, Marchese G, Biamino S, Mirzadeh H (2020) Hot deformation behavior and flow stress modeling of Ti–6Al–4V alloy produced via electron beam melting additive manufacturing technology in single β-phase field. Mater Sci Eng A 792:139822. https://doi.org/10.1016/j.msea.2020.139822
8. Abdi A, Ashany JZ, Fatemi S (2019) Effect of powder density and energy density on the process parameters of laser melted parts. In: 16th Annual and 5th International Conference on Manufacturing Engineering (ICME2019)
9. Gibson I, Rosen D, Strucker B (2015) Additive manufacturing technologies, 3D printing, rapid prototyping, and direct digital manufacturing. Springer, New York, NY. https://doi.org/10.1007/978-1-4939-2113-3
10. Sames WJ, List FA, Pannala S, Dehoff RR, Babu SS (2016) The metallurgy and processing science of metal additive manufacturing. Int Mater Rev 61:315–360
11. Mosallanejad MH, Niroumand B, Aversa A, Manfredi D, Saboori A (2020) Laser Powder bed fusion in-situ alloying of Ti-5%Cu alloy: process-structure relationships. J Alloys Compd 857:157558. https://doi.org/10.1016/j.jallcom.2020.157558
12. Ghanavati R, Lannunziata E, Norouzi E, Bagherifard S, Iuliano L, Saboori A (2023) Design and development of SS316L-IN718 functionally graded materials via laser powder bed fusion. Mater Lett 349:134793. https://doi.org/10.1016/j.matlet.2023.134793
13. Tang M, Pistorius PC, Narra S, Beuth JL (2016) Rapid solidification: selective laser melting of AlSi10Mg. Jom 68:960–966

14. Khairallah SA, Anderson AT, Rubenchik A, King WE (2016) Laser powder-bed fusion additive manufacturing: physics of complex melt flow and formation mechanisms of pores, spatter, and denudation zones. Acta Mater 108:36–45. https://doi.org/10.1016/j.actamat.2016.02.014
15. Bandekhoda MR, Mosallanejad MH, Atapour M, Iuliano L, Saboori A (2023) Investigation on the potential of laser and electron beam additively manufactured Ti–6Al–4V components for orthopedic applications. Met Mater Int. https://doi.org/10.1007/s12540-023-01496-6
16. Srivatsan TS, Sudarshan TS (2015) Additive manufacturing: innovations, advances, and applications. CRC Press
17. Aristizabal M, Jamshidi P, Saboori A, Cox SC, Attallah MM (2020) Laser powder bed fusion of a Zr-alloy: tensile properties and biocompatibility. Mater Lett 259:126897. https://doi.org/10.1016/j.matlet.2019.126897
18. European Commission, CO2 emission performance standards for car and vans (2020 onwards), (2020). https://climate.ec.europa.eu/
19. Kastensson Å (2014) Developing lightweight concepts in the automotive industry: taking on the environmental challenge with the SåNätt project. J Clean Prod 66:337–346. https://doi.org/10.1016/j.jclepro.2013.11.007
20. Aluminium demand in automotive sector to more than double by 2025: Novelis' Labat, (2018) visited on November 2022. https://www.reuters.com
21. Li W, Li S, Liu J, Zhang A, Zhou Y, Wei Q, Yan C, Shi Y (2016) Effect of heat treatment on AlSi10Mg alloy fabricated by selective laser melting: microstructure evolution, mechanical properties and fracture mechanism. Mater Sci Eng A 663:116–125
22. Lewandowski JJ, Seifi M (2016) Metal additive manufacturing: a review of mechanical properties. Annu Rev Mater Res 46:151–186
23. Kusoglu IM, Gökce B, Barcikowski S (2020) Research trends in laser powder bed fusion of Al alloys within the last decade. Addit Manuf 36:101489
24. Aversa A, Marchese G, Saboori A, Bassini E, Manfredi D, Biamino S, Ugues D, Fino P, Lombardi M (2019) New aluminum alloys specifically designed for laser powder bed fusion: a review. Materials (Basel) 12:1007
25. Subbiah R, Bensingh J, Kader A, Nayak S (2020) Influence of printing parameters on structures, mechanical properties and surface characterization of aluminium alloy manufactured using selective laser melting. Int J Adv Manuf Technol 106:5137–5147
26. Trevisan F, Calignano F, Lorusso M, Pakkanen J, Aversa A, Ambrosio EP, Lombardi M, Fino P, Manfredi D (2017) On the selective laser melting (SLM) of the AlSi10Mg alloy: process, microstructure, and mechanical properties. Materials (Basel). 10:76. https://doi.org/10.3390/ma10010076
27. Lee JA, Chen PS (2004) Aluminum-scandium alloys: material characterization, friction stir welding, and compatibility with hydrogen peroxide (MSFC Center Director's Discretionary Fund Final Report, Proj. No. 04–13 at NASA Marshall Space Flight Center)
28. Palm F (2018) Aluminum material having improved precipitation hardening. US20150027595A1
29. Griffiths S, Rossell MD, Croteau J, Vo NQ, Dunand DC, Leinenbach C (2018) Effect of laser rescanning on the grain microstructure of a selective laser melted Al-Mg-Zr alloy. Mater Charact 143:34–42
30. Croteau JR, Griffiths S, Rossell MD, Leinenbach C, Kenel C, Jansen V, Seidman DN, Dunand DC, Vo NQ (2018) Microstructure and mechanical properties of Al-Mg-Zr alloys processed by selective laser melting. Acta Mater 153:35–44
31. SCALMALLOY®RP Auminum-magnesium-scandium alloy powder, Visited on November 2022. https://www.voxelmatters.com
32. Schmidtke K, Palm F, Hawkins A, Emmelmann C (2011) Process and mechanical properties: applicability of a scandium modified Al-alloy for laser additive manufacturing. Phys Procedia 12:369–374
33. Spierings AB, Dawson K, Voegtlin M, Palm F, Uggowitzer PJ (2016) Microstructure and mechanical properties of as-processed scandium-modified aluminium using selective laser melting. Cirp Ann 65:213–216
34. Awd M, Tenkamp J, Hirtler M, Siddique S, Bambach M, Walther F (2018) Comparison of microstructure and mechanical properties of Scalmalloy®produced by selective laser melting and laser metal deposition. Materials (Basel) 11:17
35. Muhammad M, Nezhadfar PD, Thompson S, Saharan A, Phan N, Shamsaei N (2021) A comparative investigation on the microstructure and mechanical properties of additively manufactured aluminum alloys. Int J Fatigue 146:106165
36. Spierings AB, Dawson K, Kern K, Palm F, Wegener K (2017) SLM-processed Sc-and Zr-modified Al-Mg alloy: mechanical properties and microstructural effects of heat treatment. Mater Sci Eng A 701:264–273
37. Yang Y, Li X, Khonsari MM, Zhu Y, Yang H (2020) On enhancing surface wear resistance via rotating grains during selective laser melting. Addit Manuf 36:101583. https://doi.org/10.1016/j.addma.2020.101583
38. Taghian M, Mosallanejad MH, Lannunziata E, Del Greco G, Iuliano L, Saboori A (2023) Laser powder bed fusion of metallic components: Latest progress in productivity, quality, and cost perspectives. J Mater Res Technol 27:6484–6500. https://doi.org/10.1016/j.jmrt.2023.11.049
39. Viale V, Stavridis J, Salmi A, Bondioli F, Saboori A (2022) Optimisation of downskin parameters to produce metallic parts via laser powder bed fusion process: an overview. Int J Adv Manuf Technol 123:2159–2182. https://doi.org/10.1007/s00170-022-10314-z
40. Ralls AM, Kumar P, Menezes PL (2021) Tribological properties of additive manufactured materials for energy applications: a review. Processes 9:31
41. Zhang H, Gu D, Yang J, Dai D, Zhao T, Hong C, Gasser A, Poprawe R (2018) Selective laser melting of rare earth element Sc modified aluminum alloy: thermodynamics of precipitation behavior and its influence on mechanical properties. Addit Manuf 23:1–12
42. Tocci M, Pola A, Girelli L, Lollio F, Montesano L, Gelfi M (2019) Wear and cavitation erosion resistance of an AlMgSc alloy produced by DMLS. Metals (Basel) 9:308
43. Lorusso M, Aversa A, Manfredi D, Calignano F, Ambrosio EP, Ugues D, Pavese M (2016) Tribological behavior of aluminum alloy AlSi10Mg-TiB2 composites produced by direct metal laser sintering (DMLS). J Mater Eng Perform 25:3152–3160. https://doi.org/10.1007/s11665-016-2190-5
44. Mishra AK, Upadhyay RK, Kumar A (2021) Surface wear anisotropy in AlSi10Mg alloy sample fabricated by selective laser melting: effect of hatch style, scan rotation and use of fresh and recycled powder. J Tribol 143(2):021701. https://doi.org/10.1115/1.4047788
45. Yang Y, Zhu Y, Khonsari MM, Yang H (2019) Wear anisotropy of selective laser melted 316L stainless steel. Wear 428:376–386
46. Bahshwan M, Myant CW, Reddyhoff T, Pham M-S (2020) The role of microstructure on wear mechanisms and anisotropy of additively manufactured 316L stainless steel in dry sliding. Mater Des 196:109076
47. ASTM International (2017) Standard test method for microindentation hardness of materials, E384–17
48. ASTM International (2005) Standard Test method for wear testing with a Pin-on-Disk apparatus, G99

49. Mosallanejad MH, Abdi A, Karpasand F, Nassiri N, Iuliano L, Saboori A (2023) Additive manufacturing of titanium alloys: processability, properties, and applications. Adv Eng Mater 2301122. https://doi.org/10.1002/adem.202301122
50. Aboulkhair NT, Everitt NM, Ashcroft I, Tuck C (2014) Reducing porosity in AlSi10Mg parts processed by selective laser melting. Addit Manuf 1–4:77–86. https://doi.org/10.1016/j.addma.2014.08.001
51. Tang M, Pistorius PC (2017) Oxides, porosity and fatigue performance of AlSi10Mg parts produced by selective laser melting. Int J Fatigue 94:192–201
52. Louvis E, Fox P, Sutcliffe CJ (2011) Selective laser melting of aluminium components. J Mater Process Technol 211:275–284
53. Gu D, Dai D (2016) Role of melt behavior in modifying oxidation distribution using an interface incorporated model in selective laser melting of aluminum-based material. J Appl Phys 120:83104
54. Maskery I, Aboulkhair NT, Corfield MR, Tuck C, Clare AT, Leach RK, Wildman RD, Ashcroft IA, Hague RJM (2016) Quantification and characterisation of porosity in selectively laser melted Al–Si10–Mg using X-ray computed tomography. Mater Charact 111:193–204
55. Rosenthal I, Stern A, Frage N (2017) Strain rate sensitivity and fracture mechanism of AlSi10Mg parts produced by selective laser melting. Mater Sci Eng A 682:509–517
56. Caiazzo F, Alfieri V, Corrado G, Argenio P (2017) Laser powder-bed fusion of Inconel 718 to manufacture turbine blades. Int J Adv Manuf Technol 93:4023–4031
57. Messler Jr RW (2008) Principles of welding: processes, physics, chemistry, and metallurgy. WILEY-VCH Verlag GmbH & Co. https://doi.org/10.1002/9783527617487
58. Spierings AB, Dawson K, Heeling T, Uggowitzer PJ, Schäublin R, Palm F, Wegener K (2017) Microstructural features of Sc-and Zr-modified Al-Mg alloys processed by selective laser melting. Mater Des 115:52–63
59. Nezhadfar PD, Thompson S, Saharan A, Phan N, Shamsaei N (2021) Structural integrity of additively manufactured aluminum alloys: effects of build orientation on microstructure, porosity, and fatigue behavior. Addit Manuf 47:102292. https://doi.org/10.1016/j.addma.2021.102292
60. Li R, Wang M, Yuan T, Song B, Chen C, Zhou K, Cao P (2017) Selective laser melting of a novel Sc and Zr modified Al-6.2 Mg alloy: processing, microstructure, and properties. Powder Technol 319:117–128
61. Spierings AB, Dawson K, Dumitraschkewitz P, Pogatscher S, Wegener K (2018) Microstructure characterization of SLM-processed Al-Mg-Sc-Zr alloy in the heat treated and HIPed condition. Addit Manuf 20:173–181. https://doi.org/10.1016/j.addma.2017.12.011
62. Dieter GE, Bacon DJ (1996) Mechanical metallurgy. McGraw-hill New York
63. Zhu Y, Zou J, Yang H (2018) Wear performance of metal parts fabricated by selective laser melting: a literature review. J Zhejiang Univ A 19:95–110
64. Kumar A, Choudhary A, Tiwari A, James C, Kumar H, Arora PK, Khan SA (2021) An investigation on wear characteristics of additive manufacturing materials. Mater Today Proc 47:3654–3660. https://doi.org/10.1016/j.matpr.2021.01.263
65. Devaraju A (2015) A critical review on different types of wear of materials. Int J Mech Eng Technol 6:77–83
66. Kang CCN, Coddet P, Liao H, Baur T (2016) Wear behavior and microstructure of hypereutectic Al-Si alloys prepared by selective laser melting. Appl Surf Sci 378:142–149
67. Bressan JD, Daros DP, Sokolowski A, Mesquita RA, Barbosa CA (2008) Influence of hardness on the wear resistance of 17–4 PH stainless steel evaluated by the pin-on-disc testing. J Mater Process Technol 205:353–359
68. Menezes PL, Nosonovsky M, Ingole SP, Kailas SV, Lovell MR (eds) (2013) Tribology for scientists and engineers: From basic to advanced concepts. Springer, New York, NY, p 948. https://doi.org/10.1007/978-1-4614-1945-7.
69. Singh R, Shadab M, Dash A, Rai RN (2019) Characterization of dry sliding wear mechanisms of AA5083/B 4 C metal matrix composite. J Brazilian Soc Mech Sci Eng 41:98
70. Wang X, Xu Y, Jackson RL (2018) Theoretical and finite element analysis of static friction between multi-scale rough surfaces. Tribol Lett 66:1–18
71. Jiménez A-E, Bermúdez M-D (2011) 2 - Friction and wear. In: Paulo Davim J (ed) Tribology for engineers. Woodhead Publishing, pp 33–63. https://doi.org/10.1533/9780857091444.33
72. Dwivedi DK (2010) Adhesive wear behaviour of cast aluminium-silicon alloys: overview. Mater Des 31:2517–2531. https://doi.org/10.1016/j.matdes.2009.11.038
73. Takadoum J (2013) Materials and surface engineering in tribology. John Wiley & Sons. https://doi.org/10.1002/9780470611524
74. Zhu Y, Zou J, Chen X, Yang H (2016) Tribology of selective laser melting processed parts: stainless steel 316 L under lubricated conditions. Wear 350:46–55
75. Whitehead JR (1950) Surface deformation and friction of metals at light loads. Proc R Soc London Ser A Math Phys Sci 201:109–124
76. Farhat ZN, Ding Y, Northwood DO, Alpas AT (1996) Effect of grain size on friction and wear of nanocrystalline aluminum. Mater Sci Eng A 206:302–313
77. Lorusso M (2009) Tribological and wear behavior of metal alloys produced by laser powder bed fusion (LPBF). In: Chowdhury MA (ed) Friction, lubrication and wear. IntechOpen. https://doi.org/10.5772/intechopen.85167
78. Rosenkranz A, Costa HL, Baykara MZ, Martini A (2021) Synergetic effects of surface texturing and solid lubricants to tailor friction and wear – a review. Tribol Int 155:106792. https://doi.org/10.1016/j.triboint.2020.106792
79. Nilsson D, Prakash B (2011) Influence of different surface modification technologies on friction of conformal tribopair in mixed and boundary lubrication regimes. Wear 273:75–81. https://doi.org/10.1016/j.wear.2011.05.002
80. Deshpande PK, Lin RY (2006) Wear resistance of WC particle reinforced copper matrix composites and the effect of porosity. Mater Sci Eng A 418:137–145
81. Hasmuni N, Ibrahim M, Raus AA, Wahab MS, Kamarudin K (2018) Porosity effects of AlSi 10 mg parts produced by selective laser melting. J Mech Eng 5(4):246–255
82. Rathod HJ, Nagaraju T, Prashanth KG, Ramamurty U (2019) Tribological properties of selective laser melted Al–12Si alloy. Tribol Int 137:94–101. https://doi.org/10.1016/j.triboint.2019.04.038
83. Otani Y, Takata N, Suzuki A, Kobashi M, Kato M (2023) Scripta Materialia microstructural origin of anisotropic tensile ductility of Al-Si alloy manufactured by laser powder bed fusion. Scr Mater 226:115259. https://doi.org/10.1016/j.scriptamat.2022.115259
84. Shifeng W, Shuai L, Qingsong W, Yan C, Sheng Z, Yusheng S (2014) Effect of molten pool boundaries on the mechanical properties of selective laser melting parts. J Mater Process Technol 214:2660–2667
85. Kim DE, Suh NP (1991) On microscopic mechanisms of friction and wear. Wear 149:199–208
86. Jackson RL (2006) The effect of scale-dependent hardness on elasto-plastic asperity contact between rough surfaces. Tribol Trans 49:135–150
87. Greer JR, Nix WD (2005) Size dependence of mechanical properties of gold at the sub-micron scale. Appl Phys A 80:1625–1629

88. Chiu C, Embury JD, Castillo T (1987) Metallography of adhesive wear in aluminum alloys. Metallography 20:99–112
89. Nimri EGM (2015) Wear mechanisms and wear investigations of dental materials; a review of the literature. Arch Oral Dent Res 2:3
90. Qin H, Xu R, Lan P, Wang J, Lu W (2020) Wear performance of metal materials fabricated by powder bed fusion: a literature review. Metals (Basel) 10:304
91. Prasada Rao AK, Das K, Murty BS, Chakraborty M (2008) Microstructure and the wear mechanism of grain-refined aluminum during dry sliding against steel disc. Wear 264:638–647. https://doi.org/10.1016/j.wear.2007.05.010
92. Avcu E (2017) The influences of ECAP on the dry sliding wear behaviour of AA7075 aluminium alloy. Tribol Int 110:173–184. https://doi.org/10.1016/j.triboint.2017.02.023
93. Li XY, Tandon KN (2000) Microstructural characterization of mechanically mixed layer and wear debris in sliding wear of an Al alloy and an Al based composite. Wear 245:148–161. https://doi.org/10.1016/S0043-1648(00)00475-0
94. Purcek G, Saray O, Kucukomeroglu T, Haouaoui M, Karaman I (2010) Effect of equal-channel angular extrusion on the mechanical and tribological properties of as-cast Zn-40Al-2Cu-2Si alloy. Mater Sci Eng A 527:3480–3488. https://doi.org/10.1016/j.msea.2010.02.019
95. Wang L, Li XX, Zhou Y, Zhang QY, Chen KM, Wang SQ (2015) Relations of counterface materials with stability of tribo-oxide layer and wear behavior of Ti–6.5Al–3.5Mo–1.5Zr–0.3Si alloy. Tribol Int 91:246–257. https://doi.org/10.1016/j.triboint.2015.01.028
96. Lim SC, Ashby MF (1987) Overview no. 55 wear-mechanism maps. Acta Metall 35:1–24